

# Short-range electrostatic screening in ionic liquids as inferred by direct force measurements

Benjamin Cross\*,<sup>1</sup> Léo Garcia,<sup>1</sup> Elisabeth Charlaix,<sup>1</sup> and Patrick Kékicheff\*<sup>2</sup>

<sup>1</sup>Université Grenoble-Alpes, CNRS, Laboratoire Interdisciplinaire de Physique, Grenoble Cedex 9 38041, France

<sup>2</sup>Institut Charles Sadron, Université de Strasbourg, CNRS UPR22, Strasbourg Cedex 2 67034, France

(Dated: March 24, 2026)

Previous experimental reports of long-range interactions in ionic liquids (ILs) stand in contradiction with theoretical predictions and numerical simulations. To provide insights into the literature discrepancies regarding the experimental ranges of electrostatic screening, claimed with orders of magnitude larger, the interactions between pairs of mica and borosilicate surfaces confining ILs are investigated by two complementary advanced Surface Force Apparatuses. Regardless of differences in confinement geometries (crossed-cylinders, sphere-flat), radii of curvature (cm–mm), and measurement techniques (stepwise versus continuous approach), two ever present force regimes are evidenced. At small surface separations, oscillatory forces reflect IL structuration and layering, while outside this gap, the interaction is monotonic repulsive. In both regimes the spatial extent and force magnitude depend critically on motion conditions, as demonstrated by achieving velocities as low as 9 pm/s with equilibration times up to 90 s. At large separations, fast surface displacements generate long-range interactions (over tens of ion size) creating the illusion of anomalous underscreening, whereas increasingly slow ones shrink both magnitude and range of the repulsion with decay-lengths converging ultimately to a screening length consistent with Poisson–Boltzmann theory with finite ion sizes. The transition from apparent long-range to short-range screening unfolds over nearly two orders of magnitude in time, revealing slow relaxation dynamics reminiscent of aging phenomena. These findings definitely resolve a decade-old controversy on force measurements and reveal rich out-of-equilibrium dynamics. The hydrodynamic contribution to the net force is admittedly crucial to be reduced especially when relaxations span decades in time, but approaching thermodynamic equilibrium during measurements proves essential.

## Significance

In electrolytes mobile ions screen electric fields all the more they are concentrated. However, in the last decade, conflicting experimental reports of long-range interactions in ionic liquids (ILs) and concentrated electrolytes have puzzled theory and numerical simulations. The discrepancy lies in nonequilibrium effects as evidenced by our rigorous measurement protocols using complementary advanced Surface Force Apparatuses. ILs screening is genuinely short-range under conditions approaching thermodynamic equilibrium. Their decay lengths ( $\sim 0.5$  nm) match the theoretical predictions. Conversely the further from equilibrium the larger interaction extents. These arise from background drift rates with various relaxations spanning two orders of magnitude in time scale. The IL behavior is reminiscent of slow relaxation dynamics in glasses, thin polymer films, historical paintings, and granular media.

## INTRODUCTION

Ionic liquids are molten salts comprising polyatomic organic or inorganic ions that melt at temperatures below 100 °C. Their cations and anions are typically of large size (5 to 10 larger than monoatomic ions), asymmetric shape with conformational flexibility, polar, polarizable, often hydrophobic [1, 2]. Unlike traditional salts, these anisotropic flexible and large structures separate cation and anion centers, lowering the ionic liquids (ILs) melting points to ambient temperature. The short-range ion–ion interactions concur with the shape and the charge distribution of ion molecules to unique IL properties. Their nonflammability, low volatility, high ion conductivity, thermal and chemical stability, enable numerous applications in bulk (catalysis, electrochemistry) and at interfaces (lubrication, electrowetting, energy storage) [3]. In confined geometries the solid interfaces may change the properties because of the IL interactions with the substrate and of a layering IL structure formation, as revealed both by molecular dynamics [4–8] and experimental techniques sensitive to molecular arrangements at interfaces, such as X-ray reflectivity [9], atomic force microscopy (AFM) [2, 10–13], or surface force apparatus (SFA) [14–31]. These interface and confinement properties, which have only been partially explored remain not fully understood.

**Author contributions:** B.C. and P.K. designed research; L.G., B.C., and P.K. performed the experiments; B.C. and P.K. analyzed data; B.C., P.K., and E.C. interpreted the results; and P.K. and B.C. wrote the paper with the input of all authors. All authors gave approval to the final version of the paper.

**Competing interests:** The authors declare no competing interest.

**Correspondence:** benjamin.cross@univ-grenoble-alpes.fr; patrick.kekicheff@ics-cnrs.unistra.fr

Published in *PNAS* **123**(7), e2517939123 (2026). doi:10.1073/pnas.2517939123

© 2026 the Author(s). Distributed under CC BY-NC-ND 4.0.

First, spontaneous phase change from liquid to solid

may occur when the IL is squeezed between solid walls into films thinner than typically 5 to 10 molecular diameters. Thus, some studies suggest ILs behave partly as solids under confinement [29, 32], while others disagree [16, 30, 33]. Second, between confining walls, beyond the short-range ordered IL layering regime perpendicular to the interfaces, most of the force measurements did not reveal any other interactions either by AFM [10–13] or SFA [14–21, 24, 25] techniques. Nevertheless, recent studies show interactions decaying exponentially at large surface separation  $D$ . These observations [mainly SFA [22, 23, 25–29, 31]; one AFM study [13]] prompted comparisons with the exponential repulsion operating at large distances in aqueous electrolytes [34–41]. The main focus was on the decay-length, identified as the screening length,  $\lambda$ , of the electrical double layer. In the limit of low concentrations, the corresponding decay-length is the Debye screening length,  $\kappa_D^{-1}$ , that decreases with the total ionic density as

$$\kappa_D^{-1} = \left( \frac{\varepsilon_0 \varepsilon_r k_B T}{\sum_j \rho_j q_j^2} \right)^{1/2} \quad (1)$$

where  $k_B$  designates the Boltzmann constant,  $T$  the temperature,  $\varepsilon_0$  the vacuum permittivity, and  $\varepsilon_r$  the relative permittivity (dielectric constant) and where the sum runs over the charged species with number density  $\rho_j$  and charge  $q_j$ . In a 1:1 electrolyte of bulk concentration  $\rho_{\text{ion}}$ , the Debye length is  $\kappa_D^{-1} = 1/\sqrt{8\pi L_B \rho_{\text{ion}}}$  with  $L_B = e^2/4\pi\varepsilon_0\varepsilon_r k_B T$  the Bjerrum length of the solvent ( $\approx 0.7$  nm for water at room temperature). When the screening length becomes comparable to the ion diameter  $a$  (bare or hydrated size), or to the mean distance between charges, the continuum approximation for the charge density becomes inappropriate and corrections to the Debye length are expected [42, 43]. Thus, a few experimental reports [26, 34, 39, 40] revealed large decay-lengths,  $\lambda$ , in concentrated aqueous electrolytes, while others did not [35–38, 41]. Furthermore,  $\lambda$  appeared to increase with ionic concentration, strongly exceeding expected  $\kappa_D^{-1}$  values [26, 34, 39, 40]. These anomalously large screening lengths in concentrated aqueous electrolytes were reunited to the other few similar IL observations, and this set, so-called “underscreening” behavior, was claimed to follow an empirical scaling relation:

$$\frac{\lambda}{\kappa_D^{-1}} \propto (a\kappa_D)^{\nu} \quad (2)$$

with  $\nu = 0$  for  $\kappa_D^{-1} > a$ , and  $\nu = 3$  for  $\kappa_D^{-1} < a$  [27].

The concept of constraint due to the ion size is evidently fruitful, especially in the case of large ions. Several theories taking into account the ions sizes have been suggested for long [42, 43], and the unexpected large underscreening behavior has motivated several recent theoretical approaches (see for instance refs. [5–7, 44] and

references therein). However, despite ingenious interpretations of Eq. (2), no theoretical model has reproduced this scaling relation. Thus, the exponent  $\nu$  is calculated to be around 2 rather than 3 in ref. [44]. Such prediction comes also along similar conclusions established by numerical simulations: “in a high density regime the ratio  $\lambda/\kappa_D^{-1}$  increases according to a power law, in qualitative agreement with experimental measurements, albeit at a much slower rate” [5]. There, the exponent  $\nu \sim 3/2$ , well below the reported 3, does evidence an underscreening behavior, that nevertheless does not lead to the suggested extent of long-range exponential repulsions with large screening lengths.

Whether these discrepancies result from theoretical limitations, simulation imperfections, or experimental shortcomings and inadequacies remains unclear. It is indeed a challenge to grasp complex processes when competing ion adsorption on charged surfaces, ion layering, cluster formation, and other electrical double layer phenomena (dynamic and structural behaviors) are involved. Elaboration of such a complex and multiparametric model can be based only on a versatile collection of information obtained by reliable sets of experimental data. Despite extensive research in concentrated aqueous electrolytes and in ILs, experimental force-distance profiles remain contradictory, both in their range and in their magnitude. Furthermore, for the observations claiming underscreening behavior, the reported screening length values exceed theoretical predictions and numerical simulations by almost one order of magnitude. This discrepancy appears puzzling and a number of questions remain unanswered. Their resolution requires further investigations, which is the object of this study.

Since ionic liquids represent the asymptotic case of concentrated electrolytes at zero dilution, we focus our study on ILs at this extreme limit where electrostatic effects are most pronounced. A rigorous experimental framework deciphers quantitatively how measurements may deviate from theoretical predictions and numerical simulations. Thus, our robust methodologies can guide further experiments across the broader spectrum of concentrated electrolytes.

We measured surface forces using two complementary advanced SFAs and two different ILs. This allowed the force-distance profiles to be compared under varied quasi-static and dynamic conditions, different confinement geometries (crossed-cylinders, sphere-plane), different materials (mica, borosilicate) with molecularly smooth surfaces of curvature spanning one order of magnitude (cm to mm). We show that consistency can be established provided two criteria are fulfilled. The hydrodynamic contribution to the net force is admittedly crucial to be reduced but of much importance, thermodynamic equilibrium must be approached during measurements.

## RESULTS AND DISCUSSION

One primary mission of our investigation is to get force-distance profiles under conditions as close as possible to thermodynamic equilibrium all the way through from large distances down to contact. The classical quasi-static SFA procedure translates the lower mica surface of the apparatus by a small amount and then allows it to come to rest (usually for no more than 10 s due to intrinsic surface drifts) at the new position, which is expected to have reached equilibrium [45]. The surface separation,  $D$ , is then recorded by interferometry and the force,  $F$ , between the two mica surfaces is calculated in the usual way, from the difference in the change in displacement of each end of the cantilever. The procedure is repeated to generate the entire force-distance profile. However, any mechanical and thermal drifts prevent genuine equilibrium position to be set at each successive step, especially when the liquid medium is viscous as ILs are. These limitations encountered in all previous SFA reports for ILs are overcome by the high stability of our advanced homemade SFA where precise nano-controlled displacement and fine variation of  $D$  allow the effective movement to be lowered down to 9 pm/s and equilibration times to be extended up to 90 s at any surface separation over a few micrometers range from contact. These experimental inputs offer a great platform for measuring IL surface forces. Thus, scan durations can last as long as  $\sim 10$  h for just a single one-way approach starting at  $D \sim 500$  nm. Over the same scan the surface motion can be actuated in a variety of traveling speeds, dwell times (surfaces left to rest over a predefined duration before the next nanosized step is initiated), and incremental steps in the range 2 to 0.2 nm (all details in SI Appendix, section 4). With this procedure, hereafter referred to “stepwise protocol”, both the surface separation and the force relax together toward their equilibrium values after each displacement step of the piezo-driven confining surface. As a consequence, the hydrodynamic contribution can be substantially reduced compared to continuous velocity methods [46] at equivalent speeds. Moreover, the challenging task of determining a no-slip plane position becomes a nonissue in the force-distance profile analysis. Thus, hydrodynamic, surface forces and structural contributions can be unraveled using this appealing procedure. On one hand, slowing down the movement reduces the hydrodynamic contribution to the force since it grows as  $1/D$  upon confinement within a macroscopic continuum Reynolds framework for film drainage [46]. Concomitantly, with surfaces better stabilized at each new gap by lengthening the equilibration time, one favors the confined IL under stress to undergo its structural rearrangements.

Figure 1 presents a series of force-distance profiles measured for the ionic liquid  $[\text{C}_2\text{mim}][\text{NTf}_2]$  (viscosity

$\eta = 37$  mPa·s and IL characteristics: see SI Appendix, Table S1) using our stepwise protocol at different velocities and resting times (all experimental parameters are detailed in SI Appendix, section 4). The qualitative designations assigned for high, fast, moderate, and very slow speeds correspond to a global run time of about 20 min, 40 min, 1.5 h, and 10 h respectively for a profile measured on approach of the two surfaces (solid symbols) over a  $\sim 500$  nm range down to their contact. These total scan durations are of course not proportional to an effective surface velocity over the entire  $D$ -range since in the oscillatory regime encountered at short separations a lot of time is taken up traveling very little or no distance. Conversely at large separations where strong short-range forces are not present, our procedure allows an average speed to be defined (values reported in the central graph). Figure 1 compares the force-distance profiles when at large separations this average speed ( $\sim 0.27$  nm/s at “high speed”; brown circles) is reduced systematically down to 0.011 nm/s at “very slow speed” (green squares). In each case a repulsive force is observed which increases in overall magnitude as the surface separation is reduced. The monotonic continuous dependence with  $D$  is broken with further confinement signaling the occurrence of an oscillatory regime. Below  $D \sim 10$  nm, the force-distance profiles appear discontinuous because of the intrinsic mechanical instability of the cantilever that supports one of the mica surfaces: when the gradient of the force is larger than the spring stiffness  $K$  (i.e.,  $\partial F/\partial D > K$ ) the system jumps from unstable to stable regimes, leaving unexplored and inaccessible regions [45]. Some of those could be recovered by measuring both the interaction upon approach (solid symbols) and separation (empty symbols) of the two surfaces, but caution is advised as the force curves differed in several ways as set out hereafter.

Both the spatial extent and form of the oscillatory regime depend on motion conditions of the mica surface that confines the IL. The slower velocity the larger extent: the first oscillations could be observed at  $D$  as large as  $\sim 8$  nm for very slow approaching surfaces but at gaps less than 5 nm at high speeds. The repulsive background on which the oscillations superpose results from the interplay of two effects. Faster movements induce larger hydrodynamic repulsions, but instead give the confined IL less time to undergo structural rearrangements and layering buildup. As a result, the compressive energy barrier to squeeze out any layer in formation is lowered and the related oscillation in the force profile reduces its height or may even disappear (more details in SI Appendix, section 5). Such scenarios already observed in other fragile systems such as sponge and lamellar mesophases [47, 48] once again underline the importance of conducting force measurements under conditions as close as possible to thermodynamic equilibrium.

Another feature is nonreversibility in the oscillatory regime upon reversal of the movement, even at the slow-



contribution as additive interactions for interpreting total measured forces.

Contrary to the hysteresis observed in the oscillatory regime the forces are reversible at separations where solvation forces are absent. Reversing the surface motion at any stage gives the same monotonic repulsion with characteristics not changing much upon approach or separation. Interestingly, the force-distance profile previously reported by Gebbie et al. [23] for the same  $[\text{C}_2\text{mim}][\text{NTf}_2]$  was reproduced when similar approach rates were used (Fig. 1, top right with  $\sim 1.5$  h for a  $\sim 500$  nm range and average speed  $\sim 0.1$  nm/s at large separations). Indeed, these authors actuated the surface displacement at constant rates of 0.2 to 1 nm/s implying that their compressive force run lasted no longer than 1 h for bringing the surfaces from  $\sim 200$  nm down to mechanical contact. It is informative to follow their data analysis by attempting the large separation regime to be described as an exponential repulsion. Within this framework a large decay-length  $\lambda = 6.8 \pm 0.3$  nm is inferred from the line of best fit to the data despite scatter and force spanning over one order magnitude only. Similar attempts of exponential fits for each velocity provide various decay-lengths, all of large values, but with a strong dependence on surface motion conditions.

Several arguments combine to not assign what would appear to be a long-range exponential repulsion to an electrostatic double-layer interaction, contrary to what was previously claimed for force profiles measured in ILs [22, 23, 25–28, 31]. First, fits to large scattered force data and besides over one order magnitude only may cast doubt on the validity of an exponential profile representation. Second, the force dependence on surface motion conditions over a regime where solvation forces are absent is at odds with a pure electrical double layer interaction. Indeed, lower velocities with concomitant longer waiting times at each new surface position reduce both magnitude and range of the repulsions. The profiles decay back to zero force at increasingly shorter distances with effective  $\lambda$ -values decreasing by more than one order of magnitude from  $\sim 11.5$  to  $\sim 0.75$  nm at the slowest possible surface displacement. The spatial extent becomes quite narrow with no measurable force detected beyond 12 nm within  $\pm 0.01$  mN/m resolution (Inset) whereas the 8 to 9 nm signals the transition to the solvation regime. With a force magnitude reduced by more than one decade, the repulsion consequently appears no longer long-ranged. The decay-length  $0.75 \pm 0.05$  nm, now close to the Debye-screening length expected for IL systems, suggests that the asymptotic repulsion arises from an electrical double layer interaction. Using the Poisson–Boltzmann (PB) equation a fit would suggest an interaction at constant potential  $|\psi| \sim 22 \pm 1$  mV boundary condition at the onset of the oscillatory regime transition. Nevertheless, caution must be taken. The presence of the ionic layers makes difficult a genuine determination of the double-

layer origin. Furthermore, in more accurate theories the screening of the charge near each surface is more effective than in the PB mean field approach. As a result, DLVO fits produce effective values smaller than the actual ones, with the only exception to this behavior occurring for electrolytes with very large counterions [50]. However, these complications in no way affect the screening length of the double-layer interaction at large separations.

To support and extend this result, additional experiments were carried out with another ionic liquid  $[\text{C}_4\text{mim}][\text{PF}_6]$ , using another surface force apparatus (dSFA, see SI Appendix), with a different geometry (sphere-plane instead of crossed-cylinders), a radius of curvature  $R$  an order of magnitude smaller and different surface materials (borosilicate instead of mica). The surface displacement system is also different, since it relies on a controlled expansion rate of the piezoelectric actuator rather than on a step movement [51, 52]. Only the repulsive regime observed at large separations is reported here as the short-range elastic and solvation parts of the interaction were discussed previously [30]. Here again, the effect on magnitude and range of the repulsion was investigated when the approach velocity of the surfaces was decreased over two orders of magnitude from 3 nm/s to 15 pm/s.

Figure 2 reveals that at the highest velocity of 3.0 nm/s, the force profile (solid blue losanges) is dominated by a hydrodynamic Reynolds behavior. The hydrodynamic force (dotted blue line) is calculated with no fitting parameter using  $\eta = 157$  mPa·s for the IL viscosity (SI Appendix, Table S1) and a no-slip plane position at  $b = 7.8 \pm 0.5$  nm (SI Appendix, Fig. S2), an inferred value that agrees with hydrodynamic measurements on similar systems [30]. Note that only the relative displacements between the surfaces are measured, and the  $D_0$  position corresponds to the hydrodynamic origin of the distances (SI Appendix, Fig. S1). This  $D_0$  determination produces only a translation of the  $D$ -axis and has no impact on the analysis of the interactions and the inferred exponential decay lengths reported below. For intermediate velocities (0.6 nm/s in green), the force profile exhibits two distinct regimes. As long as the surface separations are sufficiently large, the measurements align perfectly with a hydrodynamic fit (dotted green line with same  $\eta$ , but  $b = 6.5 \pm 0.5$  nm, Fig. 2). However, as  $D$  is reduced below 15 nm the force profile deviates from a pure hydrodynamic behavior indicating the competition with an additional repulsion, that is further analyzed below. At the lowest approaching velocity of 0.015 nm/s, the repulsion (black circles) is short-ranged (no measurable force detected beyond  $\sim 8$  nm within the rms  $F/R$  resolution limit equal to 0.03 mN/m) with a magnitude much larger than hydrodynamics (dotted black line).

To analyze further the force profiles, hydrodynamics and any other possible contributions are considered as purely additive interactions. Thus, the nonhydro-

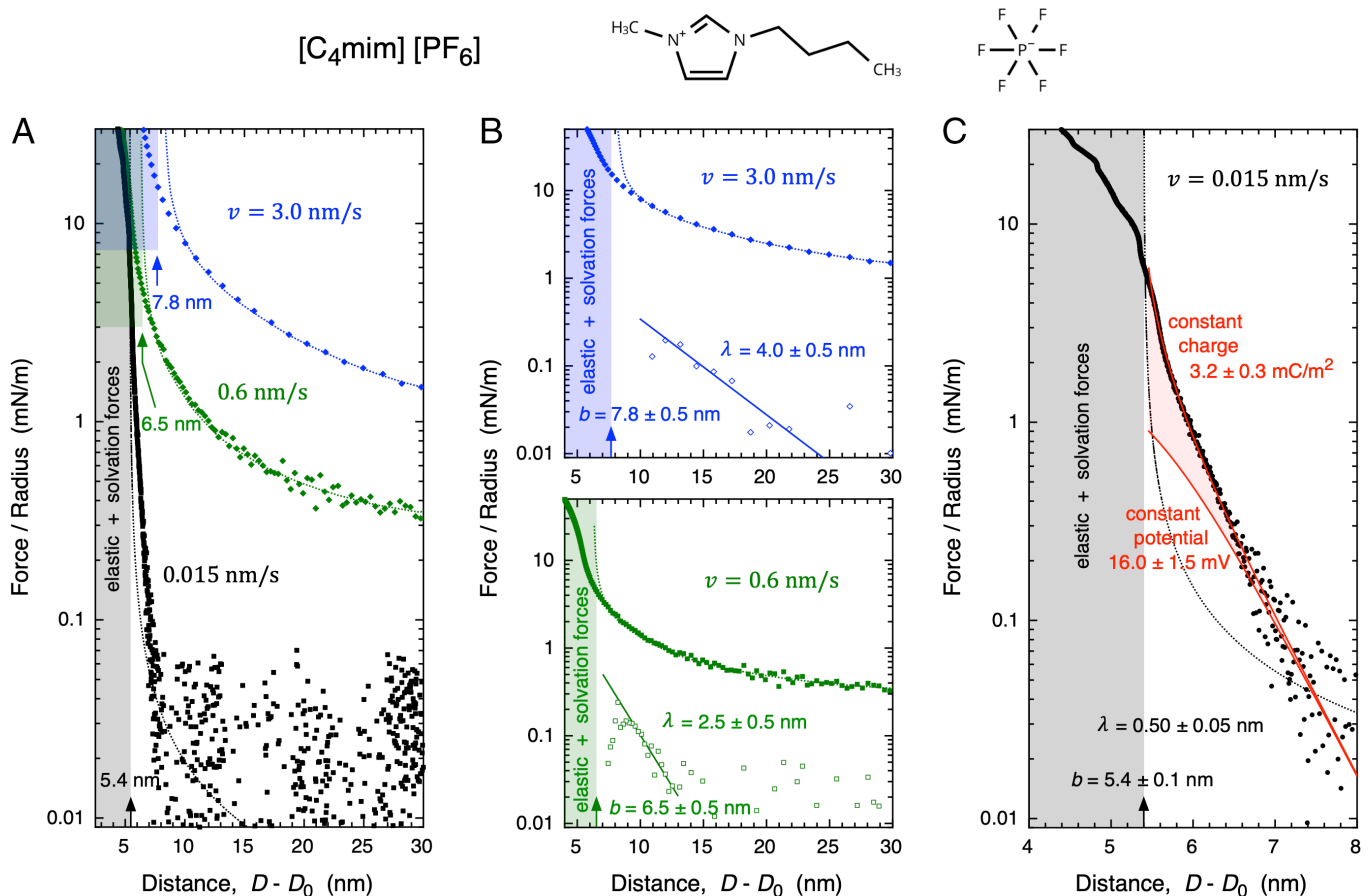


FIG. 2. Force-distance profiles of butyl-1-methyl-3-imidazolium [C<sub>4</sub>mim]<sup>+</sup> hexafluorophosphate [PF<sub>6</sub>]<sup>-</sup> between borosilicate surfaces in a flat-sphere (radius  $R = 3.3$  nm) geometry. (A) Solid symbols are the measured forces at different approaching surface velocities  $v = 3.0$  (blue),  $0.6$  (green), and  $0.015$  nm/s (black) while dotted lines represent the calculated corresponding hydrodynamic force (SI Appendix, Figs. S2 and S3). (B) Beyond the elastic and solvation forces regime (gray zone), the nonhydrodynamic interactions (open symbols), inferred by subtracting the hydrodynamics from the total measured force at  $v = 3.0$  and  $0.6$  nm/s, could appear as having exponential profiles with decay-lengths  $\lambda = 4.0 \pm 0.5$  nm and  $2.5 \pm 0.5$  nm respectively. (C) At the slowest velocity  $v = 0.015$  nm/s, the total interaction is short-range, exponentially decaying with  $\lambda = 0.50 \pm 0.05$  nm close to the expected screening length for the IL, with a double-layer interaction at constant charge boundary condition.

dynamic component can be inferred by subtracting the hydrodynamic contribution (dotted line) from the total measured forces (solid symbols) as reported by open symbols in Fig. 2B. This additional interaction is tempted to be described by an exponential profile despite scattered data that furthermore span over one-order of force magnitude only. Thus, fitted decay-lengths  $\lambda = 4.0 \pm 0.5$  nm and  $2.5 \pm 0.5$  nm would be inferred respectively at the highest  $3.0$  nm/s and intermediate  $0.6$  nm/s velocity.

Conversely, at the smallest  $0.015$  nm/s velocity, the force profile exhibits a pure exponential behavior over two orders of magnitude (Fig. 2C) with no need of any hydrodynamic subtraction being much weaker. Its decay-length  $\lambda = 0.50 \pm 0.05$  nm is once again close to the Debye-screening length expected for IL systems, suggesting that the asymptotic exponential repulsion arises from a double layer interaction. In this distance regime, the

van der Waals attraction is weak [ $F/R_{vdW} = -A/6D^2$  neglecting retardation and electrolyte screening effects on the effective Hamaker constant  $A \sim 0.8 \times 10^{-20}$  J between borosilicate substrates across the IL [37, 53]]. The profile is then fitted using a numerical solution of the non-linearized PB equation for constant charge and constant potential boundary conditions. With the same caution taken beforehand for marking the electrical double layer onset at the transition with the oscillatory regime, the double-layer repulsion follows a constant surface charge interaction  $|\sigma| = 3.2 \pm 0.3$  mC/m<sup>2</sup>, a value in good agreement with theoretical predictions [54], whereas the surface potential  $|\psi| = 16.0 \pm 1.5$  mV amounts to a comparable value for the other IL investigated differently with the other SFA.

Regardless of differences in ILs, surface materials, and confinement geometries, both IL datasets demonstrate

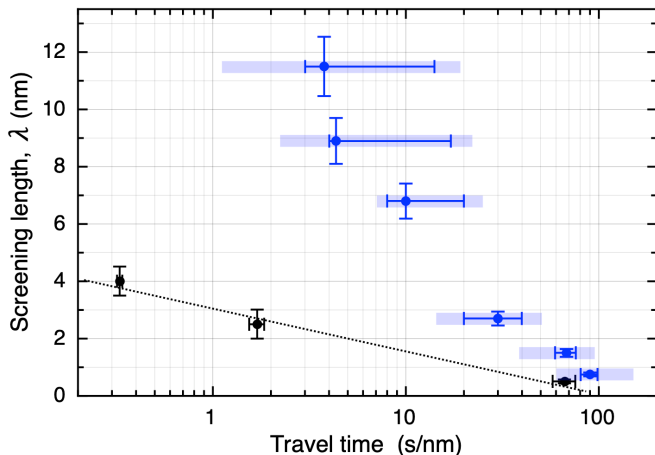


FIG. 3. Evolution of the apparent screening length,  $\lambda$ , of the monotonic repulsion at large separations (from Figs. 1 and 2) as a function of travel time (inverse of approach velocity). Blue symbols represent  $[\text{C}_2\text{mim}][\text{NTf}_2]$  confined between crossed mica cylinders of radii of curvature  $R \sim 10$  to  $20$  nm (all experimental parameters reported in SI Appendix, Fig. S4) using the stepwise protocol set for conventional SFA, while black symbols correspond to  $[\text{C}_4\text{mim}][\text{PF}_6]$  between borosilicate surfaces in a sphere-flat geometry ( $R = 3.3$  nm) measured with the dSFA. Regardless of different ILs, surface materials, experimental configurations and protocols, both datasets show a steady decrease of  $\lambda$  from  $\sim 12$  nm at high velocities (short travel times) down to  $0.5$  to  $0.75$  nm under quasi-static conditions (long travel times  $\tau \sim 100$  s/nm). Error bars are uncertainties on  $\lambda$  inferred from the fits and  $\tau$ -ranges of displacement increments used along the measured monotonic repulsion only (SI Appendix, section 4), while shadowy blue rectangles indicate the full  $\tau$ -ranges used over the entire force-distance profile; the dotted line serves as a guide to the eye. Through two independent techniques and different ILs, the semilogarithmic representation reveals that the relaxation extends over two orders of magnitude in time scale, underscoring the IL slow progressive approach toward equilibrium. Thus, by allowing sufficient time for the confined systems to approach their equilibrium state, the decay lengths converge toward the theoretically predicted screening length.

that the screening length decreases steadily over two orders of magnitude in travel time, dropping by more than one decade from  $\sim 12$  nm at the fastest down to  $\sim 0.5$  to  $0.75$  nm at the slowest motion conditions (Fig. 3). There, the measured  $\lambda$  are of the order of the ion sizes  $a$  (SI Appendix, Table S1), with  $\lambda/a \approx 0.68$  to  $1.25$  for  $[\text{C}_2\text{mim}][\text{NTf}_2]$  and  $\approx 0.83$  to  $1.08$  for  $[\text{C}_4\text{mim}][\text{PF}_6]$  representing short-range screening consistent with the theoretical predictions by Attard [42] and Janeček and Netz [43]. The fact that  $\lambda$  exceeds  $\kappa_{\text{D}}^{-1}$  by  $\sim 10$  reflects the well-known finite-size corrections at high concentrations but remains far from the anomalous “underscreening” regime previously reported by others (where  $\lambda/\kappa_{\text{D}}^{-1}$  ratios up to  $\sim 200$  were claimed). Both investigated ILs are in a regime where  $\lambda/a > \kappa_{\text{D}}^{-1}/a$  remains well below

the Fisher–Widom threshold of  $\sqrt{6} \approx 2.45$ , whether one considers the Debye length  $\kappa_{\text{D}}^{-1}$  or our measured screening length  $\lambda$ . In such a regime, the theoretical framework predicts an exponential (rather than oscillatory) decay of the charge–charge correlations at large separations together with no transition to complex screening parameters [42, 43]. This is precisely what we observe under quasi-static measurement conditions. The oscillatory forces observed at short range ( $D < 8$  to  $10$  nm) reflect the structural layering of ILs at interfaces rather than oscillatory electrostatic screening. These solvation forces arise from the molecular structure of the liquid under confinement—a distinct phenomenon from the charge–charge correlations discussed in refs. [42, 43]. The periodicity of these oscillations ( $\sim 0.8$  nm) corresponds to ion-pair dimensions, confirming their structural origin. In addition, the increase in surface layer thicknesses with slower motions suggest that incomplete structural reorganization could explain the observed deviations from equilibrium, possibly related to capillary solidification [29].

This study demonstrates that ionic liquid screening is short-range under quasi-static conditions approaching thermodynamic equilibrium. Such a conclusion would not have been possible if the experimental framework for measuring force–distance profiles was not fulfilled twofold. First, the use of two complementary techniques using most advanced setups allows new procedures for accurate measurements. Second, perturbations of the confined IL with transient structures at the surface are also controlled and minimized once thermodynamic equilibrium is reached. To fulfill this goal, a rigorous and suitable protocol with two main experimental cautions was developed: slow velocity for the moving surface, long equilibration times between successive positions, all together with a subnano-controlled way of the continuous varying thickness of the confined gap. This twofold remark also leads to get insights into the entangled contributions of hydrodynamic and surface forces to the total measured interaction. Once the importance of measurements under conditions approaching thermodynamic equilibrium is recognized, the previous confused puzzle of wildly varying observations can be rationalized. Our direct force measurements reconcile at last the predictions set by theory and numerical simulations. The proposed methodology sets the bases of a solid ground to pursue for collecting valuable information concerning fine details of the electrolytes behavior at elevated concentrations upon confinement.

Our investigation confirms the existence of a long-range force that could approach a decaying exponential with distance. Nevertheless, its related decay length,  $\lambda$ , is a strong function of travel time (the inverse of the velocity) as revealed in Fig. 3. The exceptional broad temporal range highlights that ILs approach equilibrium upon confinement through slow, progressive transitions rather than sharp ones. Such extended relaxation dy-

namics spanning multiple time decades are reminiscent of aging-like phenomena observed in a variety of systems, including polymer films [55–59], historical paintings [60], granular media [61]. Thus, structural relaxation can extend over years [55–59] or centuries [60] at ambient temperature with equilibration times strongly dependent on film thickness and interfacial interactions [55–58, 61]. In nanoscale polymer films, slow dynamics are associated with hierarchical energy landscapes that offer a variety of pathways for spatial and time relaxation through dynamical heterogeneities. As a consequence, measurements were shown to depend critically on equilibration protocols: insufficient waiting times lead to artifacts and contradictory observations [58]. While the microscopic origins of the slow dynamics in confined ILs may differ from those in polymer glasses, the phenomenological similarity—extended relaxation over logarithmic time scales and strong sensitivity to measurement protocols—suggests that future investigations could benefit from concepts and theoretical frameworks developed for these other interfacial systems.

The finding that screening dynamics in confined ionic liquids span multiple time decades fundamentally challenges equilibrium-based descriptions of these systems. Unraveling the physical origin of this temporal complexity—whether structural frustration, precursors to phase transitions, or novel mechanisms—represents a critical frontier for understanding charge transport in nanoconfined electrolytes and optimizing next-generation energy storage devices.

## MATERIALS AND METHODS

Force-distance profiles were measured between pairs of atomically smooth mica and borosilicate surfaces confining two aprotic ionic liquids based on methylimidazolium cations: 1-ethyl-3-methylimidazolium bis-(trifluoromethylsulfonyl)imide  $[\text{C}_2\text{mim}][\text{NTf}_2]$  and butyl-1-methyl-3-imidazolium hexafluorophosphate  $[\text{C}_4\text{mim}][\text{PF}_6]$  at 25 °C. Two complementary homemade advanced surface force apparatus (SFA) were employed. One is based on the conventional SFA technique [45] operating with backsilvered mica surfaces in a crossed-cylinder geometry using multiple-beam interferometry (FECO) for distance measurement,  $D$ . The high stability of our setup allows the moving surface to be stepwise translated by a nano-controlled displacement and then left to rest over a predefined duration before the next nanosized step is actuated. Quasi-static equilibrium conditions can thus be approached with effective slow movements as low as 9 pm/s and equilibration times extended up to 90 s at any surface separation over a few micrometers range from contact. The second complementary setup (dSFA) provides force-distance profiles like conventional SFA but also characterizes

the linear harmonic force response of the thin films confined between borosilicate surfaces in a sphere-flat configuration. Both the relative surface displacement and the deflection of a flexure hinge are simultaneously monitored by Nomarski interferometry under continuous approach [51, 52]. With surface velocities that can be varied over two orders of magnitude (from 3 down to 0.015 nm/s) rate-dependent effects can be distinguished from equilibrium interactions. Detailed experimental procedures are provided in the Supplementary Information. These include materials characterization, distance calibration protocols, hydrodynamic analysis, and how the different force contributions to the total force can be disentangled.

*Data availability.* All study data are included in the article and/or SI Appendix. Raw experimental data files have been deposited in Zenodo [62].

## ACKNOWLEDGMENTS

Romain Lhermerout is gratefully acknowledged for discussions on the hydrodynamic aspects of ionic liquids under confinement. The project was supported by the French National Research Agency (ANR) through Grant No. ANR-19-CE30-0012. Technical development of the advanced quasi-static Surface Force Apparatus benefited from the experimental work carried out within the framework of the MICASOL platform set between Institut Charles Sadron, CNRS, Strasbourg, France, and SOLEIL synchrotron radiation facility, France (<https://www.ics-cnrs.unistra.fr/micasol>).

- 
- [1] M. Armand, F. Endres, D. R. MacFarlane, H. Ohno, and B. Scrosati, *Nat. Mater.* **8**, 621 (2009).
  - [2] R. Hayes, G. Warr, and R. Atkin, *Chem. Rev.* **115**, 6357 (2015).
  - [3] M. V. Fedorov and A. A. Kornyshev, *Chem. Rev.* **114**, 2978 (2014).
  - [4] R. M. Lyndell-Bell *et al.*, *Acc. Chem. Res.* **40**, 1138 (2007).
  - [5] B. Rotenberg, O. Bernard, and J.-P. Hansen, *J. Phys.: Condens. Matter* **30**, 054005 (2018).
  - [6] S. W. Coles *et al.*, *J. Phys. Chem. B* **124**, 1778 (2020).
  - [7] J. Zeman, S. Kondrat, and C. Holm, *J. Chem. Phys.* **155**, 204501 (2021).
  - [8] R. J. E. Reinertsen *et al.*, *Proc. Natl. Acad. Sci. U.S.A.* **121**, e2316537121 (2024).
  - [9] M. Mezger *et al.*, *Science* **322**, 424 (2008).
  - [10] R. Atkin *et al.*, *Phys. Chem. Chem. Phys.* **13**, 6849 (2011).
  - [11] O. Werzer, E. D. Cranston, G. G. Warr, R. Atkin, and M. W. Rutland, *Phys. Chem. Chem. Phys.* **14**, 5147 (2012).
  - [12] N. Hjalmarsson, R. Atkin, and M. W. Rutland, *J. Phys. Chem. C* **120**, 26960 (2016).

- [13] N. Hjalmarsson, R. Atkin, and M. W. Rutland, *Chem. Commun.* **53**, 647 (2017).
- [14] R. G. Horn, D. F. Evans, and B. W. Ninham, *J. Phys. Chem.* **92**, 3531 (1988).
- [15] S. Perkin, T. Albrecht, and J. Klein, *Phys. Chem. Chem. Phys.* **12**, 1243 (2010).
- [16] K. Ueno, M. Kasuya, M. Watanabe, M. Mizukami, and K. Kurihara, *Phys. Chem. Chem. Phys.* **12**, 4066 (2010).
- [17] I. Bou-Malham and L. Bureau, *Soft Matter* **6**, 4062 (2010).
- [18] S. Perkin *et al.*, *Chem. Commun.* **47**, 6572 (2011).
- [19] S. Perkin, *Phys. Chem. Chem. Phys.* **14**, 5052 (2012).
- [20] A. M. Smith *et al.*, *J. Phys. Chem. Lett.* **4**, 378 (2013).
- [21] A. M. Smith, K. R. J. Lovelock, and S. Perkin, *Faraday Discuss.* **167**, 279 (2013).
- [22] R. M. Espinosa-Marzal, A. Arcifa, A. Rossi, and N. D. Spencer, *J. Phys. Chem. C* **118**, 6491 (2014).
- [23] M. A. Gebbie, H. A. Dobbs, M. Valtiner, and J. N. Israelachvili, *Proc. Natl. Acad. Sci. U.S.A.* **112**, 7432 (2015).
- [24] H.-W. Cheng *et al.*, *Adv. Mater. Interfaces* **2**, 1500159 (2015).
- [25] A. M. Smith and S. Perkin, *J. Phys. Chem. Lett.* **6**, 4857 (2015).
- [26] A. M. Smith, A. A. Lee, and S. Perkin, *J. Phys. Chem. Lett.* **7**, 2157 (2016).
- [27] A. A. Lee, C. S. Perez-Martinez, A. M. Smith, and S. Perkin, *Faraday Discuss.* **199**, 239 (2017).
- [28] M. A. Gebbie *et al.*, *Chem. Commun.* **53**, 1214 (2017).
- [29] J. Comtet *et al.*, *Nat. Mater.* **16**, 634 (2017).
- [30] L. Garcia, L. Jacquot, E. Charlaix, and B. Cross, *Faraday Discuss.* **206**, 443 (2018).
- [31] R. Lhermerout and S. Perkin, *Phys. Rev. Fluids* **3**, 014201 (2018).
- [32] S. Chen, G. Wu, M. Sha, and S. Huang, *J. Am. Chem. Soc.* **129**, 2416 (2007).
- [33] R. Göbel *et al.*, *Phys. Chem. Chem. Phys.* **11**, 3653 (2009).
- [34] R. M. Pashley and J. N. Israelachvili, *J. Colloid Interface Sci.* **97**, 511 (1984).
- [35] R. M. Pashley and J. N. Israelachvili, *J. Colloid Interface Sci.* **101**, 446 (1984).
- [36] R. M. Pashley, *J. Colloid Interface Sci.* **102**, 23 (1984).
- [37] V. E. Shubin and P. Kékicheff, *J. Colloid Interface Sci.* **155**, 108 (1993).
- [38] P. Kékicheff, S. Marčelja, T. J. Senden, and V. E. Shubin, *J. Chem. Phys.* **99**, 6098 (1993).
- [39] T. Baimpos, B. R. Shrestha, S. Raman, and M. Valtiner, *Langmuir* **30**, 4322 (2014).
- [40] P. Gaddam and W. Ducker, *Langmuir* **35**, 5719 (2019).
- [41] S. Kumar *et al.*, *J. Colloid Interface Sci.* **622**, 819 (2022).
- [42] P. Attard, *Phys. Rev. E* **48**, 3604 (1993).
- [43] J. Janeček and R. Netz, *J. Chem. Phys.* **130**, 074502 (2009).
- [44] R. M. Adar, S. A. Safran, H. Diamant, and D. Andelman, *Phys. Rev. E* **100**, 042615 (2019).
- [45] J. N. Israelachvili and G. E. Adams, *J. Chem. Soc. Faraday Trans. 1* **74**, 975 (1978).
- [46] D. Y. C. Chan and R. G. Horn, *J. Chem. Phys.* **83**, 5311 (1985).
- [47] E. Freyssingeas, D. Antelmi, P. Kékicheff, P. Richetti, and A.-M. Belloq, *Eur. Phys. J. B* **9**, 123 (1999).
- [48] L. Herrmann, A. Johner, and P. Kékicheff, *Phys. Rev. Lett.* **113**, 268302 (2014).
- [49] Z. Wang, H. Li, R. Atkin, and C. Priest, *Langmuir* **32**, 8818 (2016).
- [50] R. Kjellander and S. Marčelja, *J. Phys. Chem.* **90**, 1230 (1986).
- [51] L. Garcia, C. Barraud, C. Picard, J. Giraud, E. Charlaix, and B. Cross, *Rev. Sci. Instrum.* **87**, 113906 (2016).
- [52] C. Barraud, L. Garcia, B. Cross, and E. Charlaix, *Meas. Sci. Technol.* **28**, 045103 (2017).
- [53] J. Mahanty and B. W. Ninham, *Dispersion Forces* (Academic Press, New York, NY, 1976).
- [54] M. Z. Bazant, B. D. Storey, and A. A. Kornyshev, *Phys. Rev. Lett.* **106**, 046102 (2011).
- [55] R. D. Priestley, C. J. Ellison, L. J. Broadbelt, and J. M. Torkelson, *Science* **309**, 456 (2005).
- [56] E. Charrault, C. Gauthier, P. Marie, and R. Schirrer, *J. Polym. Sci. B, Polym. Phys.* **46**, 1337 (2008).
- [57] S. Napolitano and M. Wübbenhorst, *Nat. Commun.* **2**, 260 (2011).
- [58] O. Bäumchen, J. D. McGraw, J. A. Forrest, and K. Dalnoki-Veress, *Phys. Rev. Lett.* **109**, 055701 (2012).
- [59] G. B. McKenna, *Rubber Chem. Technol.* **93**, 79 (2020).
- [60] L. Bratasz, K. G. Akoglu, and P. Kékicheff, *Herit. Sci.* **8**, 11 (2020).
- [61] L. Bocquet, E. Charlaix, S. Ciliberto, and J. Crassous, *Nature* **396**, 735 (1998).
- [62] B. Cross, L. Garcia, E. Charlaix, and P. Kékicheff, Supporting data for “Short-range electrostatic screening in ionic liquids as inferred by direct force measurements”, Zenodo, <https://doi.org/10.5281/zenodo.18391727> (2026), deposited 29 January 2026.

**Supporting Information for:**  
***Short-range electrostatic screening in ionic liquids***  
***as inferred by direct force measurements***

Benjamin Cross,<sup>1,\*</sup> Léo Garcia,<sup>1</sup> Elisabeth Charlaix,<sup>1</sup> and Patrick Kékicheff<sup>2,†</sup>

<sup>1</sup>*Université Grenoble-Alpes, CNRS, Laboratoire Interdisciplinaire de Physique, Grenoble Cedex 9 38041, France*

<sup>2</sup>*Institut Charles Sadron, Université de Strasbourg,  
CNRS UPR22, Strasbourg Cedex 2 67034, France*

**CONTENTS**

Materials	1
Force measurement procedures	1
Analysis of dSFA measurements	3
Hydrodynamic origin of distances	3
No-slip plane position	5
Analysis of conventional SFA measurements	6
Interplay of hydrodynamic and surface forces contributions	12
Effect on the structural forces	12
Hydrodynamic vs. electrostatic force contributions	14
References	16

**MATERIALS**

Two common aprotic ionic liquids, both based on methylimidazolium cations, but with different anions are compared. The cations differ by the length of their hydrophobic alkyl chain, 1-ethyl-3-methylimidazolium, abbreviated as [C<sub>2</sub>mim]<sup>+</sup>, and butyl-1-methyl-3-imidazolium noted [C<sub>4</sub>mim]<sup>+</sup> (or [Bmim]<sup>+</sup>), whereas their associated anions are bis-(trifluoromethylsulfonyl)imide ([NTf<sub>2</sub>]<sup>-</sup>) and hexafluorophosphate [PF<sub>6</sub>]<sup>-</sup> respectively. The [C<sub>2</sub>mim][NTf<sub>2</sub>] and [C<sub>4</sub>mim][PF<sub>6</sub>] compounds were all obtained from Solvionic (France), and used without further purification. The [C<sub>2</sub>mim][NTf<sub>2</sub>] was dried under vacuum at 100 °C for two days before deposition as a droplet (50–100 μL) in between the two confining extended cylinders of the SFA. Dry nitrogen was flowed through the gas-tight injection port of the setup at a pressure higher than the ambient atmospheric pressure for a few hours before the apparatus was resealed. All experiments were performed at 25 °C in the presence of a separate communicating reservoir located inside the sealed chamber containing desiccant phosphorous pentoxide (P<sub>2</sub>O<sub>5</sub>). Each experiment lasted between 24 and 72 h, and the P<sub>2</sub>O<sub>5</sub> reservoirs were found to be unsaturated at the completion of each experiment.

Table S1 summarizes the characteristics for these ionic liquids, as collected from literature.

**FORCE MEASUREMENT PROCEDURES**

Due to the atomic resolution in surface separation accessible, the Surface Force Apparatus (SFA) technique [17, 18] allows a direct measurement of the interaction between two macroscopic solid bodies or extended surfaces (of cm<sup>2</sup> area) confining a liquid as a function of their separation. Force-distance profiles determination reduces to the measurement of two quantities sets, namely, the force of interaction,  $F$ , between the two bodies, and the width of the gap,  $D$ , that separates them. Thus, the measurements are carried out keeping the chemical potential of all the chemical entities in the liquid constant. For the ionic liquids investigated in this work, the force-distance profiles were measured by means of two homemade advanced SFA versions with enhanced spatial and time resolution and automation, as described in

TABLE S1. Characteristics at 25 °C for the two investigated ionic liquids [C<sub>2</sub>mim][NTf<sub>2</sub>] and [C<sub>4</sub>mim][PF<sub>6</sub>].

		[C <sub>2</sub> mim] <sup>+</sup> [NTf <sub>2</sub> ] <sup>-</sup>	[C <sub>4</sub> mim] <sup>+</sup> [PF <sub>6</sub> ] <sup>-</sup>
Molecular weight $M$ (g/mol)		391.3	284.2
Viscosity $\eta$ (mPa·s)		37 <sup>[a]</sup>	157 <sup>[a]</sup>
Density $\rho$ (g/cm <sup>3</sup> )		1.52 <sup>[b]</sup>	1.37 <sup>[b]</sup>
Ionic density $\rho_{\text{ion}}$ (mol/L)		3.88 <sup>[c]</sup>	4.82 <sup>[c]</sup>
Structural sizes (nm)	Cation (nm)	$0.99 \times 0.50 \times 0.34$ <sup>[d]</sup>	$1.20 \times 0.60 \times 0.35$ <sup>[d]</sup>
	Anion (nm)	$1.15 \times 0.48 \times 0.46$ <sup>[d]</sup>	0.59 (diam.) <sup>[e]</sup>
	Avg. ion pair size $a$	0.81 <sup>[f]</sup>	0.75 <sup>[f]</sup>
	Corr. dist. between like-ions	0.90 <sup>[g]</sup>	0.63–0.66 <sup>[h]</sup>
	Nanoscale heterogeneities	expected <sup>[i]</sup>	1.2 <sup>[i]</sup>
Relative dielectric constant $\epsilon_r$		12.3 <sup>[j]</sup>	11.4 <sup>[j]</sup>
Debye length $\kappa_D^{-1}$ (nm)		0.061 <sup>[k]</sup>	0.053 <sup>[k]</sup>
Refractive index		1.422–1.423 <sup>[l]</sup>	1.417 <sup>[l]</sup>

[a] Viscosity values for [C<sub>2</sub>mim][NTf<sub>2</sub>] [1, 2] and for [C<sub>4</sub>mim][PF<sub>6</sub>] [1].

[b] Density at atmospheric pressure inferred from experiments [2, 3] and coarse molecular dynamics simulations for [C<sub>4</sub>mim][PF<sub>6</sub>] [4].

[c] Ionic density calculated as  $\rho_{\text{ion}} = \rho/M$ .

[d] Dimensions estimated from the van der Waals radii of the constituent atoms.

[e] [PF<sub>6</sub>]<sup>-</sup> anion size diameter from WAXS and numerical simulations [5].

[f] Average ion pair size  $a$  calculated from the density of the IL, assuming the packing fraction  $\chi = (\pi/6)\rho a^3$  of 0.64. This value corresponds to random packing of spheres [6] — an assumption taken by Lee et al. [7] having noted that the packing fraction is roughly constant for ionic liquids [8].

[g] Correlation distance between two cations or between two anions inferred from WAXS and WANS for [C<sub>2</sub>mim][NTf<sub>2</sub>] [9].

[h] Correlation distance between two cations in [C<sub>4</sub>mim][PF<sub>6</sub>] of 0.63 nm inferred by WAXS [10] and of 0.66 nm inferred from WANS [11].

[i] Nanoscale structural heterogeneities arising from the segregation of alkyl tails into oily domains that are embedded in a charged, three-dimensional network [12]. They were evidenced in [C<sub>4</sub>mim][PF<sub>6</sub>] [13] but not clearly detected in [C<sub>2</sub>mim][NTf<sub>2</sub>] [14].

[j] Relative dielectric constant for [C<sub>2</sub>mim][NTf<sub>2</sub>] [15] and for [C<sub>4</sub>mim][PF<sub>6</sub>] [15, 16].

[k] Debye screening length,  $\kappa_D^{-1} = (\epsilon_0 \epsilon_r k_B T / 2 \rho_{\text{ion}} e^2)^{1/2}$  calculated under the assumption that all ions are free and behave as effective charge carriers (full dissociation);  $k_B$  designates the Boltzmann constant,  $T$  the temperature,  $\epsilon_0$  the vacuum permittivity,  $\epsilon_r$  the relative permittivity (dielectric constant) and  $e$  the elementary charge.

[l] Refractive index at the sodium line ( $\lambda_D = 589.3$  nm) for [C<sub>2</sub>mim][NTf<sub>2</sub>] [2, 3] and for [C<sub>4</sub>mim][PF<sub>6</sub>] [3].

detail elsewhere [19–22]. One is based on the initial version of the Tabor-Israelachvili SFA [17, 18] using the crossed cylinder geometry of two back-silvered atomically smooth thin mica sheets (1–3  $\mu\text{m}$ ) glued down on hemicylinders (radius of curvature  $R = 10$ –20 mm) aligned at right angles [17, 18, 21, 22]. The other SFA, on which one can measure the linear harmonic force response of a thin film and, for this reason, is named dynamic Surface Force Apparatus (dSFA) [19, 20] uses a sphere ( $R = 3.3$  mm)–flat geometry with atomically smooth borosilicate surfaces (roughness measured by atomic force microscopy of  $\sim 0.2$  nm over a 100  $\mu\text{m}$  squared scan). In both devices, one surface is rigidly coupled to the force sensor (lower hemicylinder held at the end of a double-cantilever spring [21, 22]; glass sphere attached to a flexure hinge [19, 20]) whereas the opposite surface (upper hemicylinder [21, 22]; planar surface [19, 20]) is mobile, allowing the separation between the two surfaces to be controlled and finely varied over a range from tens of micrometers down to molecular contact by means of a piezo element superimposed on the coarse positioning range of a motorized micropositioner.

In both SFAs the surface separation measurement is determined by interferometry. In the conventional SFA, the optical thickness of the medium between the mica surfaces is measured with multiple-beam interferometry [23–25]. The two partly silvered mica sheets, glued silvered side down onto the surface of two glass cylinders, form an optical cavity into which white light is directed [17, 18]. Multiple reflections are undergone between the two metallic surfaces (silver 50 nm thick; reflectivity  $>98\%$  in the green region of the visible spectrum). Only certain wavelengths of the transmitted light have appreciable intensity: the spectrum is comprised of a series of fringes of equal chromatic order (FECO) [23] whose wavelengths are related to the thickness and the refractive index of each layer in the interferometer (mica sheets, confined liquid) [21, 24–26]. Standard matrix multiplication methods were used to determine the coefficients of reflection and transmission for any combination of layers widths of specified optical properties at varying wavelengths, and consequently fringe positions could be deduced [21, 22, 26, 27]. The outcome is that an absolute zero determination in separation can be determined to about 0.1 nm by bringing the two bare atomically smooth mica surfaces into contact. The comparison of this initial situation and where an IL is sandwiched shows shifts in FECO wavelengths, from which the optical thickness of the confined IL medium can be determined. Both width and refractive index can thus be inferred simultaneously [24–26]. The surface separation,  $D$ ,

is determined to within 0.2 nm whereas the refractive IL index was found to be independent of  $D$  at  $\pm 0.01$  with a value close to the bulk value reported in literature (Table S1, ref. 1).

In the dSFA, one order higher resolution (typically 20 pm) is obtained as both the relative displacement of the mobile surface and the deflection of the flexure hinge are independently measured by means of Nomarski interferometers [20]. Note that the absolute zero separation is not directly determined, but rather a hydrodynamic origin (see hereafter, Sec. 3.1). Anyway, the valuable independent determination of both surface separation,  $D$ , and force,  $F$ , is of great value in the dSFA contrary to the conventional SFA, in which the cantilever deflection (and hence  $F$ ) is calculated in the usual way, as the difference between the expected and observed deflection of the cantilever spring, i.e. from the deviation of the driving distance calibration determined at large separations by multiple beam interferometry where interaction surface forces are negligible [17, 18, 21, 22]. Another advantage of the dSFA setup is its intrinsic rigidity allowing large forces up to several hundreds of mN/m to be measured as well as mechanical deformation of the surfaces to be investigated [19, 20]. With a flexure hinge stiffness of  $\sim 5000$  N/m, the resolution in force is 0.1  $\mu$ N giving a normalized force  $F/R$  to be measured within 0.03 mN/m. In the conventional SFA, the converse situation is encountered: the cantilever spring stiffness chosen not too rigid (50–200 N/m) allows the smallest normalized force to be detected to within 0.003 mN/m, while the maximum reliably measurable force will depend on the mechanical compressibility of the entire system. Typically, surface deformations occur for applied loads larger than 8–15 mN/m [28, 29] and  $F/R$  becomes meaningless due to the deformation of the glue beneath the mica sheet; for that reason, data are only reported for smaller loads. Through the use of the Derjaguin approximation [30], the force normalized by the local radius of curvature of the surfaces,  $F/R$ , may be related to the free energy interaction per unit area between two parallel, flat surfaces,  $E$ :

$$\frac{F_{\text{crossed-cylinders}}}{2\pi R} = \frac{F_{\text{sphere-flat}}}{2\pi R} = E \quad (\text{S1})$$

since for the separation range considered ( $D \lesssim 1 \mu\text{m}$ ) the distance between the surfaces is equivalent to that between a sphere and a flat plate (since  $D/R \lesssim 3 \times 10^{-4}$  typically throughout an experiment) [30].

In both devices, repulsive forces are seen as a continuous deflection away from contact and are limited only by the onset of deformation of the surfaces evoked here before. This deflection technique is not suitable for the measurement of strongly attractive surface interactions because of the mechanical instability which occurs when the slope of the attraction exceeds the spring constant of the force measuring device. As a consequence, the technique allows forces to be measured only over the regions where the gradient of the force  $|\partial F/\partial D|$  is smaller than the spring constant  $K$ . In these measurements only parts of the force curves are directly accessible and the force vs. distance profile appears discontinuous, with jumps from unstable (i.e.  $|\partial(F/R)/\partial D| > K/R$ ) to stable mechanical regimes. Use of stiffer cantilever springs would increase the range of stability, but were not used as they were at the expense of sensitivity in measuring the force.

## ANALYSIS OF DSFA MEASUREMENTS

In dSFA measurements, the independent determination of both surface separation and force allows a detailed analysis of the different contributions to the total measured force. This section describes the successive determination of the reference frames for distance measurements (hydrodynamic origin, Sec. 3.1) and for the no-slip plane positions (Sec. 3.2). The conditions for reliably separating surface forces from hydrodynamic contributions are addressed in Sec. 5.2.

### Hydrodynamic origin of distances

A procedure that drives the two surfaces toward each other at constant speed can partially overcome the aforementioned restriction. This approach enables continuous recording of both repulsive and attractive surface forces, as previously demonstrated in many systems using the classical SFA technique [31] and in ionic liquids (ILs) using the dSFA ( $[\text{C}_4\text{mim}][\text{PF}_6]$  in ref. [32]). At very large separations, the surfaces approach each other with uniform velocity. However, at smaller separations, the cantilever supporting one surface begins to deflect as intermolecular forces emerge. The hydrodynamic force is calculated using a macroscopic continuum Reynolds framework for film drainage, using the bulk value of the viscosity  $\eta = 157$  mPa·s for  $[\text{C}_4\text{mim}][\text{PF}_6]$  (Table S1, ref. 1).

The high sensitivity of the dSFA allows a hydrodynamic origin of the distances,  $D_0$ , to be set with a 1 nm resolution using a sinusoidal flow. Thus, a sinusoidal displacement at frequency  $f$  and amplitude  $d_1$  is superimposed

on the continuous linear approach via the piezoelectric device (Fig. S1). The oscillations are maintained at values smaller than the nominal film thickness  $D - D_0$  (typically less than  $0.01(D - D_0)$ ) to ensure a linear response and to avoid perturbing the quasi-equilibrium state (experimentally confirmed). The superimposed sinusoidal displacement induces an oscillatory flow within the film, generating a pressure field on the sphere that produces a sinusoidal force at frequency  $f$  with amplitude  $F_1$  and phase shift  $\varphi$  relative to the displacement.

The experimentally measured damping coefficient  $\alpha$  corresponds to the ratio  $F_1 \sin \varphi / d_1$ . Within a linear regime with no-slip boundary conditions at the solid-liquid interface, the inverse viscous damping  $1/\alpha = (D - D_0) / (12\pi^2 \eta R^2 f)$  increases linearly with the liquid film thickness [20]. Figure S1 illustrates this relationship during continuous reduction of the gap between the two borosilicate surfaces confining the  $[\text{C}_4\text{mim}][\text{PF}_6]$  ionic liquid at a constant driving speed of 0.6 nm/s in the dSFA.

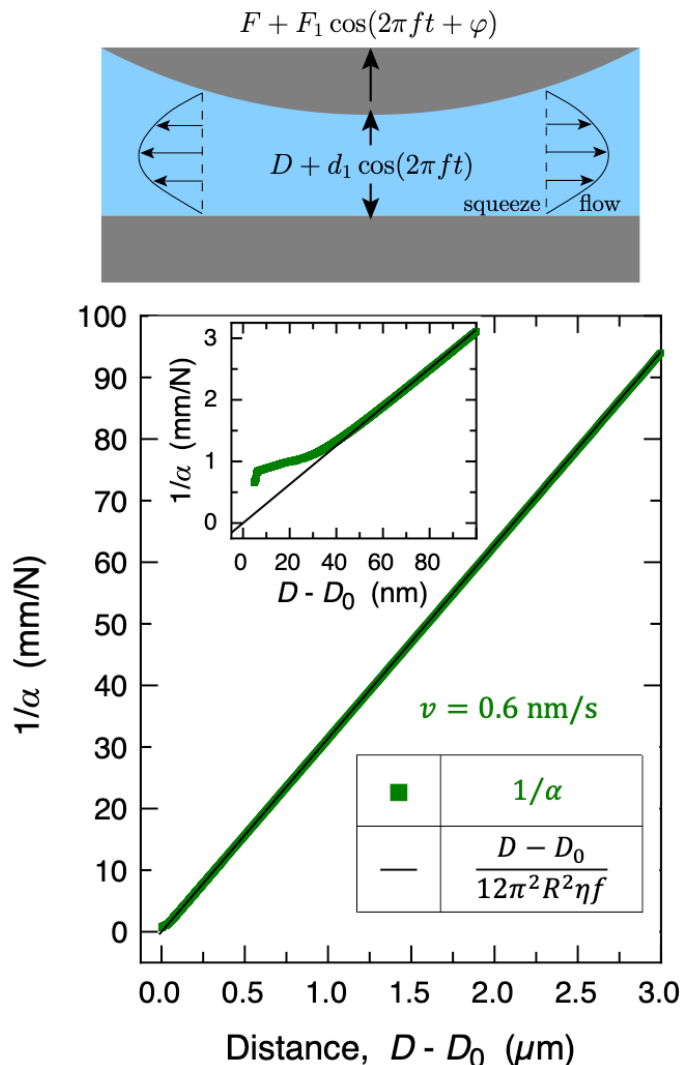


FIG. S1. Determination of the hydrodynamic origin  $D_0$ . *Top*: Schematic illustration of a dSFA experiment with  $[\text{C}_4\text{mim}][\text{PF}_6]$  showing the various measured quantities. *Bottom*: Inverse damping coefficient  $1/\alpha$  as a function of surface separation (green squares). The hydrodynamic origin distance  $D_0$  is determined by the intersection of the linear fit (black solid line, with  $\eta = 157$  mPa·s,  $R = 3.3$  mm, and  $f = 220$  Hz) with the distance axis. *Inset*: Enlargement of the data at short separations showing the deviation from the linear behavior below 50 nm due to the elasto-hydrodynamic response caused by finite surface compliance.

As evidenced in Figure S1, there is a considerable distance regime over which surface forces are negligible: the force-distance profile conforms well to the theoretical predictions for drainage of thin liquid films between extended solid surfaces. At large separations, the linear behavior results from two contributions only: the dominant hydrodynamic force and the considerably much weaker van der Waals attraction. However, a measurable deviation comes out when

the gap thickness falls below approximately 50 nm. This departure from linearity over this small distance range results from an elasto-hydrodynamic response of the confined viscous film, as it will be analyzed further below.

### No-slip plane position

At this stage, it is essential to examine how the elastic surface layers (adsorbed IL) may significantly affect the interfacial hydrodynamics. To this end, it is necessary to determine the positions of the no-slip plane, denoted as  $b$ , for drainage flows at all velocities used in the reported experiments. When a sphere and a plane undergo a relative perpendicular motion at velocity  $v$ , Stokes forces become significant. Thus, the ratio between the velocity and the force (normalized by its radius of curvature), namely  $v/(F/R)$ , will follow a linear relationship with the distance as  $(D - D_0 - b)/(6\pi\eta R)$ , at least at large separations where the hydrodynamic interactions dominate. Figures S2 illustrate this expected behavior for the velocities  $v = 3$  nm/s (blue dots) and  $v = 0.6$  nm/s (green dots). The same Figures also report the experimental data  $2\pi f R/\alpha$  using the damping coefficient used to determine  $D_0$  (squares in blue for  $v = 3$  nm/s and in green for  $v = 0.6$  nm/s). These data align along a straight line (black dotted line: linear fit carried out for film thicknesses larger than 100 nm) whose slope corresponds precisely to that of the drainage quantity  $v/(F/R)$ . This slope, given by the ratio  $1/(6\pi\eta R)$ , remains independent of the surface separation, demonstrating that the liquid film has a constant viscosity regardless of its thickness with the same value as in the bulk kept down to the shear plane. Although the two data sets exhibit identical slopes, their linear extrapolations intercept the separation axis at markedly different points. The shift between these separation intercepts directly corresponds to the no-slip plane onset  $b$ , allowing a precise experimental determination of its position:  $b = 7.8 \pm 0.5$  nm and  $6.5 \pm 0.5$  nm at respectively  $v = 3$  and 0.6 nm/s (Fig. S2 insets). At the lowest velocity  $v = 0.015$  nm/s, the hydrodynamic determination of  $b$  is not feasible because the hydrodynamic contribution is not dominant. Therefore, an alternative approach was adopted: the position of  $b$  was established by setting it at the point where structural solvation forces begin, an onset coinciding with the location of the adsorbed layers on the borosilicate substrates.

The difference between  $D_0$  determined from sinusoidal measurements and  $b$  obtained from continuous hydrodynamic analysis on the same experiment indicates the presence of an IL layer that responds to oscillatory flow while remaining immobile during steady drainage flow [32]. While these layers remain immobile under continuous drainage conditions, they actively participate in the dynamic response of the system. The elasto-hydrodynamic calculation [33] for a viscous film confined between two elastic extended solid surfaces is reported as the solid red line in Figure S2. The numerical calculation assumes a bulk viscosity value for the IL ( $\eta = 157$  mPa·s) and Young's modulus of 64 GPa for each borosilicate surface and 18 MPa for each coated layer 3.5 nm thick. Although this calculation cannot capture all the details at short separations over the ultimate 50 nm range, it successfully reproduces the main behavior of the system under harmonic excitation. Thus, the hydrodynamic plane position  $b$  appears to correspond to twice the coated layer thickness (each layer contributes to  $b/2$ ), and the elastic modulus value is consistent with previous direct surface force measurements [32].

Since the  $D_0$  determination only translates the  $D$ -axis without affecting the interaction analysis presented in the main text, all force profiles are presented as a function of the relative surface displacement.

The possibility that liquid viscosities are enhanced in very thin films and deviate from their bulk values near surfaces has been debated in the literature for decades. The current consensus appears to rule out distance-dependent viscosity functions from solid interfaces [34]. The liquid is therefore assumed to maintain a constant viscosity up to the shear plane, though this plane need not coincide with the physical surface (as exemplified in Fig. S2). This plausible approach avoids invoking microscopic explanations for enhanced viscosity near solid surfaces [35, 36], instead following the simpler framework proposed in the pioneering work of Chan and Horn [31]: an immobile liquid region exists adjacent to each solid surface during continuous drainage flow. As these authors stated: "this very simple-minded approach has two advantages. First, it introduces only one adjustable parameter [ $b$ ] with which to fit the experimental results, and second, it leaves the viscosity  $\eta$  independent of separation."

One can systematically compare results across different velocities by normalizing the measured force  $F$  by the velocity of the moving surface (Figure S3). At first approximation, all experimental data appear to fall onto a single master curve, regardless of whether the driving speed is maintained strictly constant over the entire distance range or varied incrementally through small step-size adjustments at specific gap separations. The renormalized force profiles lie on a single curve: this suggests a remarkable degree of similarity in the surface interactions across the IL film, seemingly independent of the hydrodynamic contribution magnitude. Such velocity-independent behavior has been previously reported by other research groups investigating similar confined IL systems (see for instance ref. [34]).

However, the persistence of small discrepancies between velocity conditions warrants cautious interpretation. These deviations, though small, correspond to out-of-equilibrium effects that are velocity-dependent (Figure 3, main text).

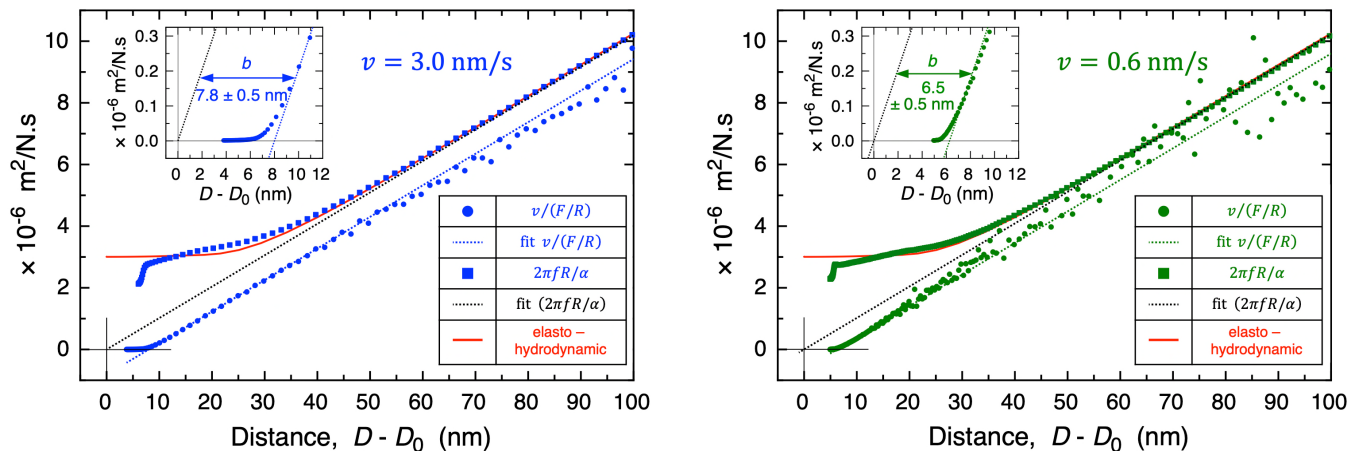


FIG. S2. Determination of the no-slip plane position for  $[C_4mim][PF_6]$  through hydrodynamic analysis at velocities  $v = 3$  nm/s (left) and  $0.6$  nm/s (right). All in blue at  $v = 3$  nm/s and in green at  $v = 0.6$  nm/s, solid circles represent the experimental data  $v/(F/R)$  for drainage at velocity  $v$ , squares are related to the harmonic quantities  $2\pi fR/\alpha$  inferred from oscillatory measurements, while dotted lines indicate the theoretical predictions. The dotted black line is a linear fit to the  $2\pi fR/\alpha$  data for film thicknesses beyond  $100$  nm, allowing  $D_0$  to be determined (see also Fig. S1). At every velocity, the identical slopes of both data sets confirm a constant viscosity independent of film thickness, while the difference in  $D$ -intercepts directly yields the no-slip plane position  $b$  (insets). The red solid line represents the elasto-hydrodynamic calculation for the confined IL between the elastic coated borosilicate surfaces.

This observation necessitates a more nuanced approach to force decomposition, as discussed in Sec. 5.1 for structural forces.

## ANALYSIS OF CONVENTIONAL SFA MEASUREMENTS

Conventional SFA measurements differ fundamentally from the continuous velocity protocols employed in dSFA experiments described in the preceding section. In usual SFA measurements [17, 18, 21], the force between the two surfaces in crossed-cylinder configuration is inferred by expanding or contracting by a predefined displacement,  $\delta$ , the piezoelectric crystal on which one surface is attached, and then measuring interferometrically the actual distance that the two surfaces have moved relative to one another,  $\Delta D$ . Any difference in the two distances when multiplied by the double-cantilever spring constant  $K$  gives, using Hooke's law, the difference between the forces at the initial and the final separations,  $\Delta F$ :

$$\Delta F = K(\delta - \Delta D) \quad (S2)$$

Using cantilevers with a spring constant,  $K$ , in the range  $50$ – $200$  N/m gives an accuracy in force of  $10$  nN, corresponding to a force normalized by radius,  $F/R$ , that could be as low as  $0.002$  mN/m for surfaces with radii of curvature,  $R$ , in the range  $10$ – $40$  mm. However, this resolution has never been attained in any SFAs, even in our advanced SFA version, despite enhanced spatial and time resolution, automation, and thermal and mechanical stability. Beyond intrinsic noise in the data measurements, the main limit arises from the uncertainty of the zero of force. Its determination is inferred from the driving distance calibration set at large separations by multiple beam interferometry [21, 22, 26] where interaction surface forces are assumed to be negligible. As a result, in this reported work, the lowest  $F/R$  value, that can be reliably measured, is about  $0.005$  mN/m.

As exemplified by Eq. (S2), the force determination analysis faces specific challenges due to the stepped displacement protocol. Because the two settings, namely, cantilever displacement (i.e. force  $F$ ) and surface separation  $D$ , cannot be handled simultaneously and measured independently upon time during the surface traveling, a genuine value of force is obtained only and only if the cantilever position is at mechanical equilibrium when the final separation is measured. Otherwise, the measure is marred by a contribution of the unrelaxed confined fluid.

One way to overcome this drawback would be to collect SFA data in the complementary situation in which a hydrodynamic force is purposely generated while being controlled and evaluated. Within this framework proposed by Chan and Horn [31], one surface is driven continuously at constant velocity and the surface forces are inferred by subtracting a calculated hydrodynamic contribution from the total measured force. In such experiments the

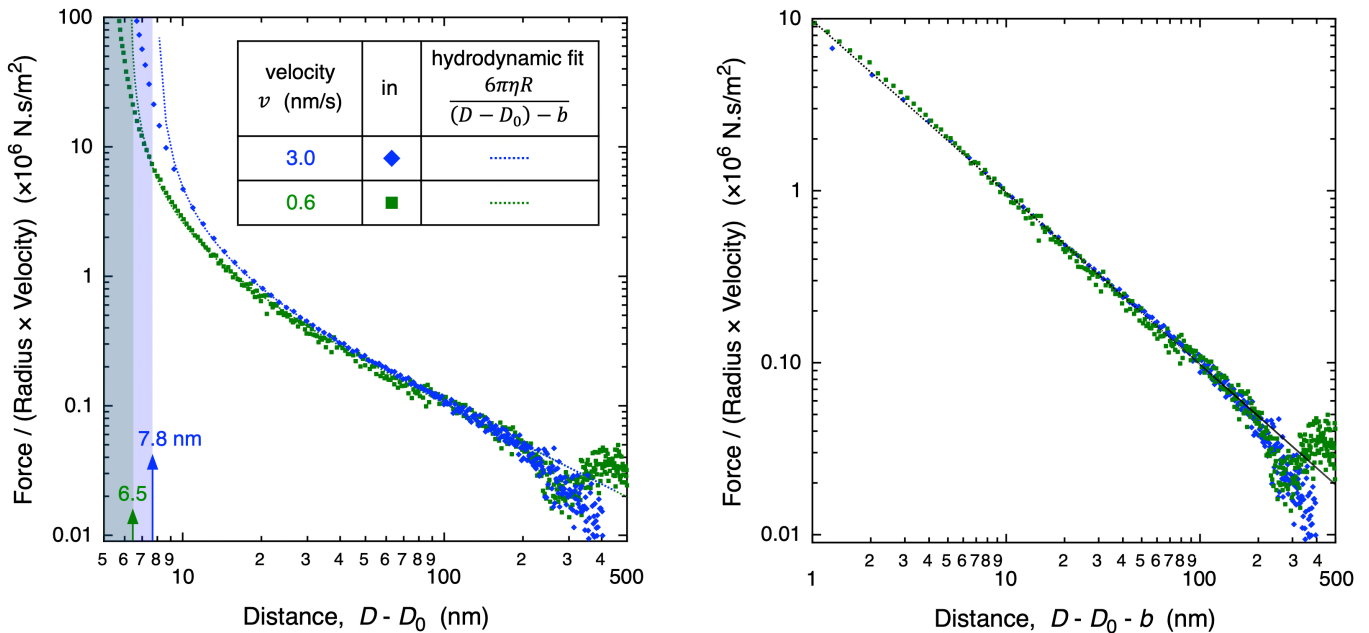


FIG. S3. Velocity-normalized force–distance profiles demonstrating near-universal scaling behavior. *Left*: Force divided by radius and velocity,  $(F/R)/v$ , as a function of the liquid film thickness  $(D - D_0)$  for two approaching velocities  $v = 3.0$  nm/s (blue diamonds) and  $0.6$  nm/s (green squares) in  $[\text{C}_4\text{mim}][\text{PF}_6]$ . Dotted lines represent hydrodynamic calculation using the theoretical expression  $6\pi\eta R/(D - D_0 - b)$ . The shadowy regions indicate the small separation range below  $10$  nm where the surface forces become significant. Vertical arrows mark the no-slip plane positions  $b$  at  $7.8 \pm 0.5$  nm (blue) and  $6.5 \pm 0.5$  nm (green) as determined in Fig. S2. *Right*: after accounting for the no-slip plane offset, the data are well described by the theoretical hydrodynamic prediction over the entire measurable range, confirming a constant viscosity behavior that is independent of film thickness, at least down to the smallest separations where surface forces dominate. Although the data merge onto a single master curve over most of the distance range, slight differences still persist at small separations as revealed in Figure 2b (main text).

hydrodynamics and any other possible contributions are considered as purely additive interactions. This method has been extremely beneficial for a variety of observations embracing different liquids and materials. Lhermerout and Perkin also applied it to ILs using carefully designed surface trajectories  $x(t)$  for modeling and inferring the position of the no-slip plane,  $b$  [37]. Their analysis demonstrated that hydrodynamic contributions were significant, while still accounting for a residual long-range interaction decaying exponentially with distance. However, in a conventional SFA an accurate determination of the IL no-slip plane position is prevented from implementing advanced protocols similar to those set in dSFA (see preceding section). As a result, any uncertainty in determining  $b$  may induce significant errors when inferring the non-hydrodynamic component through subtraction, beyond the inherent questionable assumption of additivity. As it is shown below, all these limitations no longer exist when the moving surface is stepwise translated by a nano-controlled displacement and then left to rest over a predefined duration before the next nanosized step is actuated. With this procedure, hereafter referred to “stepwise protocol”, the relaxation of the confined liquid can take place after each thickness change of the gap separating the two surfaces. As a consequence, the hydrodynamic contribution can be substantially reduced compared to continuous velocity methods at equivalent speeds. Moreover, the challenging task of determining a no-slip plane position,  $b$ , becomes a non-issue in the force-distance profile analysis.

The stepwise SFA protocol remains of value provided the surface separation change is quasi-static, that is the measurement is carried out close to thermodynamic equilibrium. To our knowledge, the quantitative assessment for which such a measurements method is valid has never been established so far. Resolution of this question requires further investigations which is the object of this section.

Driven by the piezoelectric actuator, the discrete displacement steps,  $\delta$ , lead to instantaneous force transients followed by exponential relaxations as the confined liquid flows. As a result, the opposite surface attached to the cantilever moves off with a motion that relaxes upon time according to its stiffness,  $K$ , and to the extent of the confining surfaces through their radii of curvature,  $R$ . For a given liquid viscosity,  $\eta$ , the motion response is nonlinear as it arises from the distance-dependent damping coefficient  $\lambda(D) = 6\pi\eta R^2/(D - b)$ , which is an inverse function

of the surface separation. This nonlinearity prevents the use of standard analytical solutions and necessitates the development of an iterative computational approach where the equation of motion is solved individually for each displacement step.

To mimic the SFA experiments reported in the main text (Figure 1), the numerical calculation considers a series of displacement steps bringing the surfaces together. Rather than continuous motion, each step is applied with an amplitude  $\delta$  ( $< 0$  for surface approach, as schematized in Fig. S4), at regular time intervals  $\tau$ . The initial surface separation is set to  $D(0)$  with point C at position  $x_C(0) = D(0)$  and the cantilever at  $x_B(0) = 0$ , representing no initial deflection.

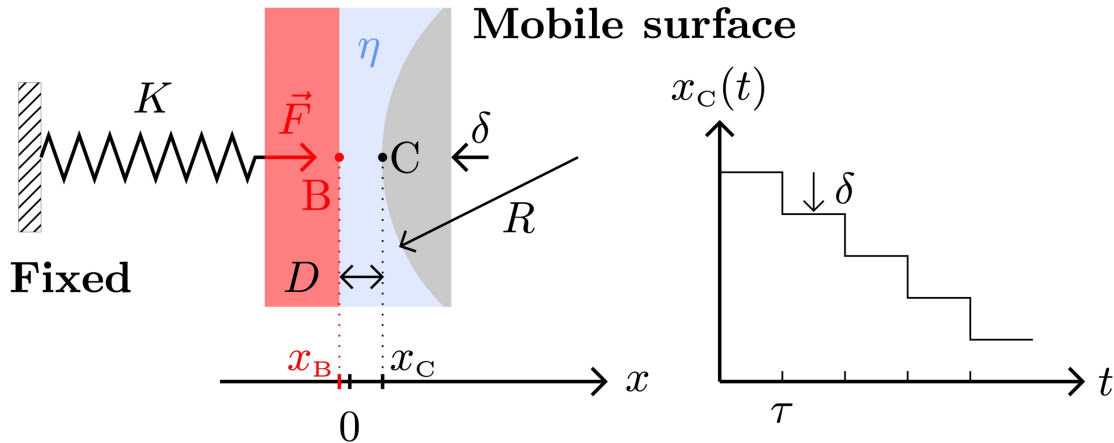


FIG. S4. Schematic representation of the nonlinear spring-damper system modeling the dynamic response of a conventional Surface Force Apparatus (SFA). The grey mobile surface carrying point C is controlled by the piezoelectric actuator, while the red surface carrying point B is connected to the cantilever attachment with spring constant  $K$ . The blue region represents the ionic liquid of viscosity  $\eta$  confined between the two mica surfaces in crossed-cylinder configuration, equivalent to a flat against a sphere of radius of curvature  $R$  [30]. The stepwise displacement is composed of incremental translations  $\delta$  of the mobile grey surface driven by the actuator at time intervals  $\tau$ . Each step increment  $\delta$  creates an instantaneous response that is then followed by an exponential relaxation of the cantilever position via a distance-dependent damping coefficient  $\lambda(D)$ .

The motion of the surface carrying the point B is governed by a force balance between the viscous Reynolds force  $F_{\text{Reynolds}} = \lambda(D) \cdot \dot{D} = \lambda(D) \cdot (\dot{x}_C(t) - \dot{x}_B(t))$  from the confined fluid and the elastic force  $F(t) = -K \cdot x_B(t)$  from the cantilever. The differential equation governing the motion of point B is then written as:

$$\lambda(D) \frac{dx_B(t)}{dt} + Kx_B(t) = \lambda(D) \frac{dx_C(t)}{dt} \quad (\text{S3})$$

The stepped displacement of point C follows  $x_C(t) = D(0) + \sum_{i=1}^N \delta \cdot H(t - (i-1)\tau)$ , where  $H$  denotes the Heaviside step function. The velocity of C consists of a series of Dirac impulses:  $dx_C(t)/dt = \sum_{i=1}^N \delta \cdot \delta_{\text{Dirac}}(t - (i-1)\tau)$ . This mathematical representation captures the essence of the experimental protocol where the discrete positioning steps create instantaneous velocity spikes followed by relaxation periods.

The surface motion response is composed of two distinct phases for each time interval  $[(i-1)\tau, i\tau]$ . During the impulse phase at each instant  $t_{i-1}$ , the Dirac impulse on C velocity is instantaneously transmitted through the damper, causing an immediate displacement of point B by the same quantity  $\delta$ . Immediately after the impulse, the B position becomes  $x_B(t_{i-1}^+) = x_B(t_{i-1}^-) + \delta$ . This instantaneous response reflects the incompressible nature of the liquid and the mechanical coupling through the hydrodynamic interaction. Between two consecutive impulses, the mobile surface attached to the actuator is immobile ( $\dot{x}_C = 0$ ), while the confined fluid and the opposite surface attached to the cantilever relaxes. Then, the differential equation reduces to  $\lambda(D) \cdot \dot{x}_B(t) + K \cdot x_B(t) = 0$ . Along this interval, we approximate  $\lambda$  as a constant equal to its previous value calculated at  $t_{i-1}^+$ , the beginning of the relaxation motion:  $\lambda_{i-1} = 6\pi\eta R^2 / [x_C(t_{i-1}^+) - x_B(t_{i-1}^+) - b]$ . This approximation is justified provided the  $\Delta D$  variation over the time interval  $\tau$  is small compared to  $D$ , which is typically satisfied in SFA measurements where displacement steps are

kept small. The movement exhibits an exponential decay with time:

$$x_B(t) = x_B(t_{i-1}^+) \exp\left[-\frac{K(t - t_{i-1})}{\lambda_{i-1}}\right] \quad (\text{S4})$$

representing the gradual relaxation of the cantilever toward its new equilibrium position.

The iterative numerical calculation proceeds sequentially through initialization with  $x_B(0) = 0$  and  $x_C(0) = D(0)$ , followed by a loop over each step  $i$  from 1 to  $N$ . At each step, the C position is updated as  $x_C(i\tau) = x_C((i-1)\tau) + \delta$ , before the instantaneous B displacement is applied  $x_B(i\tau^+) = x_B(i\tau^-) + \delta$ . The new separation is then calculated,  $D_i = x_C(i\tau^+) - x_B(i\tau^+)$ , with a concomitant determination of the damping coefficient  $\lambda_i = 6\pi\eta R^2/(D_i - b)$ . Finally, at the end of step  $i$ , the cantilever deflection  $x_B(t)$  is  $x_B((i+1)\tau^-) = x_B(i\tau^+) \exp(-K\tau/\lambda_i) = (x_B(i-1) + \delta) \exp(-K\tau/\lambda_i)$ .

The experimentally measured force corresponds to  $F_i = -K \cdot x_B(t)$ , directly relating the cantilever deflection to the applied load. The numerical calculation is terminated when  $D_i - b$  approaches the molecular dimensions of the ionic liquid (typically  $\sim 1$  nm) to avoid unphysical divergence of the viscous damping coefficient.

This iterative approach captures the essential nonlinear coupling that cannot be represented through a simple superposition of distance steps. Rather, the step-by-step calculation reveals how the system response depends critically on the instantaneous surface separation, with shorter distances producing stronger damping and slower relaxation dynamics. At large separations where  $\lambda$  is small (weak damping), the exponential relaxation is rapid and the cantilever quickly approaches its equilibrium position. Conversely, at small separations where  $\lambda$  becomes large (strong damping), the relaxation is considerably slower. This dependency creates a complex feedback mechanism where the force response to each displacement step influences the damping for subsequent steps.

The methodology provides a theoretical framework for understanding force transients often observed in SFA measurements, particularly when surfaces are approached through discrete positioning steps rather than continuous motion. These spurious transients were previously observed in a wide variety of systems, particularly in complex fluids and in materials comprising nanostructures, such as those reported in our previous investigations including surfactant aqueous solutions and lyotropic liquid crystals [38–43], polyelectrolytes [44–46], nanocolloids and nanocapsules [47–50]. The transients appear as overshoots in force measurements that gradually decay to steady-state values—a behavior that cannot be captured by static force models or linear dynamic approximations. The nonlinear damping creates a velocity-dependent apparent stiffening of the system, where rapid approach rates may result in measured forces that significantly exceed equilibrium values.

Comparison with experimental data requires careful consideration of the time scales involved. The relaxation time constant  $\tau_{\text{rel}} = \lambda/K$  varies dramatically with surface separation, potentially ranging from milliseconds at large separations to seconds or minutes at molecular-scale confinement gaps. This variation has important implications for experimental protocol design, as insufficient waiting times between successive displacement steps can lead to cumulative errors in force measurement. The iterative calculation allows optimization of step sizes and dwell times to ensure that measurements approach true equilibrium values while maintaining reasonable experimental duration for collecting data.

Figure S5 illustrates these numerical predictions for the hydrodynamic contribution to the measured force in a simple liquid having the same viscosity  $\eta = 37$  mPa·s as the IL (Table S1, refs. 1 and 2) investigated here by means of conventional SFA, namely [C<sub>2</sub>mim][NTf<sub>2</sub>].

Experimentally the force sensitivity is increased when surfaces with larger radii (lower curvatures) are used. This was the strategy implemented by Gebbie et al. who recorded force profiles for the same IL with  $R$  up to 40–50 nm [51]. Concomitantly the sensitivity is also improved with softer cantilevers ( $K$  in the range 200–50 N/m). However, increasing  $R$  enhances the viscous force (as the drag force  $F_{\text{hydro}}$  scales with  $R^2$ ) and decreasing  $K$  reduces the restoring force and increases relaxation times (Fig. S5a). These two conclusions are clearly outlined by Eq. (S4), stating that the mechanical equilibrium of the cantilever is achieved at each step by an exponential relaxation with a characteristic time scaling as  $R^2/KD$ . As a consequence of these antagonistic unfavorable conditions that both increase the hydrodynamic component, a completely opposite experimental framework must be set: surfaces with small radii and stiff cantilevers. Because these two choices go together against force sensitivity in SFA experiments, a reasonable compromise must be called for. Its search is illustrated in Figure S5a for different sets ( $K$ ,  $R$ ). There, the force profiles were calculated using regular intervals  $\tau = 20$  s for bringing the surfaces together by constant displacement increments  $\delta = 2$  nm over the full surface separation range. Note that this parameter set ( $\delta = 2$  nm,  $\tau = 20$  s) is typical of the collected data presented in the main text.

More precisely, Figure S5b reveals the full range of hydrodynamic responses across the experimental protocols presented in Figure 1 of the main text. The force profiles are calculated using the same respective spring constant,  $K$ , and radius of curvature,  $R$ , of the reported experiments (Table of Fig. S5b). The “high speed”, “fast speed” and “moderate speed” protocols were performed with almost similar  $R \sim 10$  nm and  $K \sim 100$  N/m, while slower protocols

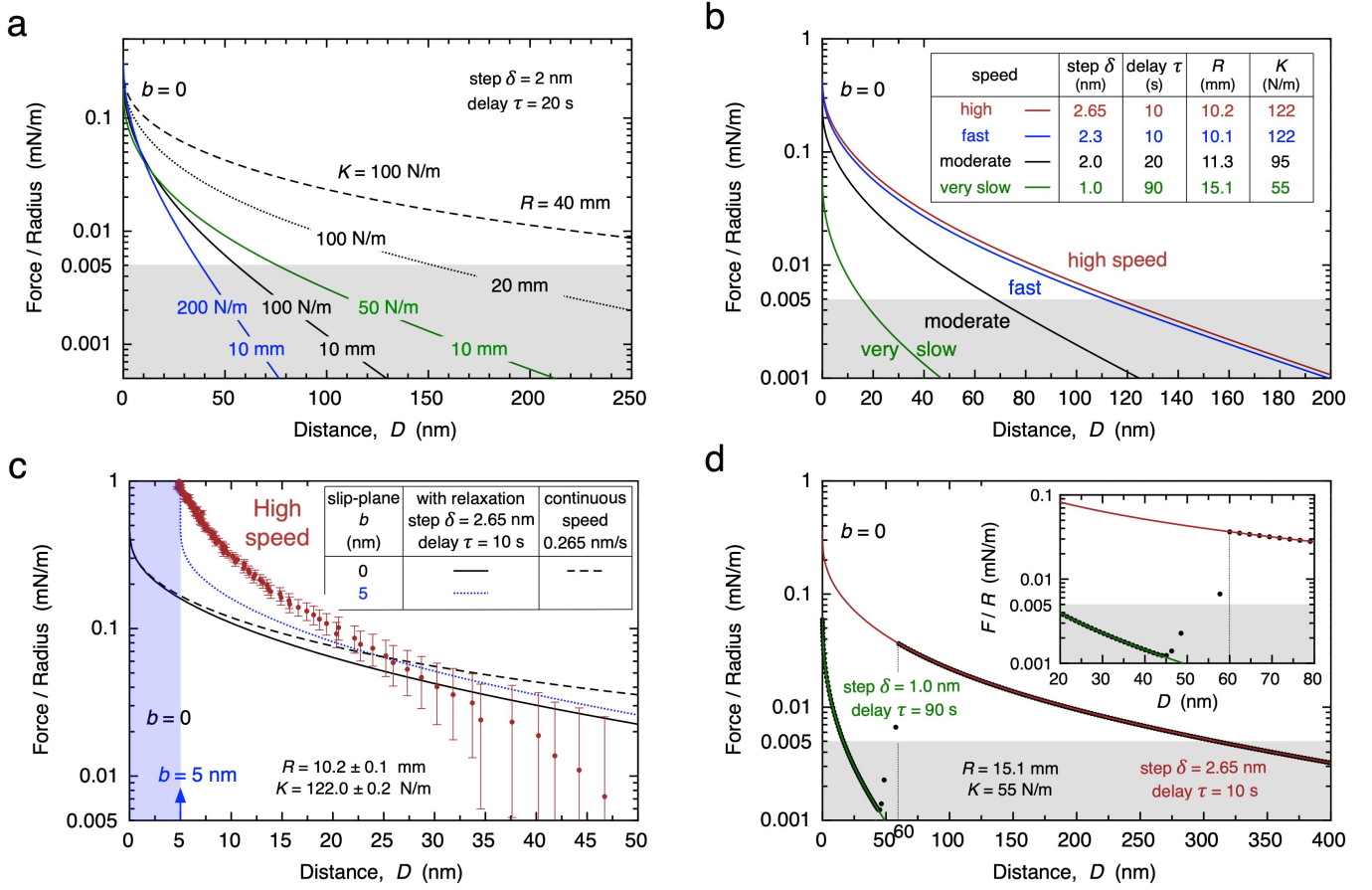


FIG. S5. Hydrodynamic force contributions in stepped displacement protocols for conventional SFA. All force-distance profiles are calculated for a simple liquid having the same viscosity  $\eta = 37$  mPa·s as the IL  $[C_2mim][NTf_2]$  investigated by means of conventional SFA (Fig. 1, main text). The hydrodynamic forces arise from their partial relaxation upon surface movement due to insufficient equilibration time,  $\tau$ , between two consecutive steps when one surface approaches the other one by incremental translations  $\delta$  (see Fig. S4). (a) Effect of cantilever spring constant  $K$  and radii of curvature  $R$  of the surfaces in crossed-cylinder geometry: the hydrodynamic contribution is reduced if the relaxation time (scaling as  $R^2/KD$  at a distance  $D$ ) is decreased, that is for larger stiffness  $K$  and smaller radii  $R$ . The grey shadowy area encompasses the experimentally inaccessible region for normalized force measurements ( $F/R < 0.005$  mN/m). (b) Hydrodynamic contributions to the total measured forces reported in Figure 1 (main text) in different protocols (“high”, “fast”, “moderate”, “very slow” speeds). All simulations are performed with the same respective experimental parameters ( $R$ ,  $K$ ) and with delays,  $\tau$ , and displacement increments,  $\delta$ , here considered as constant over the full surface separation range. The  $(\delta, \tau)$  parameters used for the numerical calculation correspond to the experimental values that were set for measuring the monotonic forces at large separations (beyond the oscillatory regime, Fig. 1). (c) Hydrodynamic force profiles calculated upon driving the surface continuously (dashed black line) or along a stepwise approach at the same effective “high” speed ( $= 0.265$  nm/s) with the no-slip plane onset located either at contact ( $b = 0$ , continuous black line) or away ( $b = 5$  nm, dotted blue line). In all cases the hydrodynamic contributions are smaller than the experimental measured forces (red dots) for  $D < 30$  nm. At larger separations, the uncertainty in force measurements calls for caution at this “high speed”. (d) Effect of switching from high velocity (at large separations) to very slow speed (at short separations). Despite a factor  $\sim 25$  in velocity reduction, the hydrodynamic forces catch up its new profile in only 3 incremental steps, outlining the absence of long-term memory effects.

were carried out with larger radii ( $R \sim 15$  mm) and softer cantilevers ( $K = 55$  N/m). Note that all simulations are calculated with delays,  $\tau$ , and displacement increments,  $\delta$ , that are constant over the full surface separation range. Their values correspond to the respective experimental ones that were set for measuring the monotonic forces at large separations (beyond the oscillatory regime, Figure 1 in main text). The simulations show that the hydrodynamic force dramatically reduces both in magnitude and range as long as one slows down the moving surface and lengthens the equilibration time between successive positions. The lowest hydrodynamic force profile is obtained when the moving surface is displaced at “very low speed”: the magnitude is below 0.01 mN/m across the entire range, essentially indistinguishable from zero given the experimental resolution. Not surprisingly, the highest forces arise at the largest

velocity (“high speed” profile).

For this “high speed” configuration, Figure S5c compares the measured forces with different simulations using the same experimental parameters but with different assumptions for positioning the no-slip plane. Regardless it is set at contact ( $b = 0$ ) or further away ( $b = 5$  nm) the experimental forces emerge significantly above both their experimental error bars and the calculated hydrodynamic profile for surfaces gap smaller than 30 nm. The observation that hydrodynamic forces are negligible below this threshold distance for the fastest velocity therefore applies *a fortiori* to all slower protocols.

The above twofold remark leads to several conclusions. First, even for relatively fast approach conditions, the choice of adequate resting times in the stepped displacement procedure allows the hydrodynamic contributions to be effectively reduced in the separation regime where monotonic repulsions have been measured. Secondly, uncertainty in the exact position of the no-slip plane—which cannot be determined as precisely in conventional SFA as in dSFA—does not weaken the analysis. Both calculations ( $b = 0$  and  $b = 5$  nm) predict force profiles with a magnitude well below the measured forces, suggesting that the monotonic (possibly exponential) regime might reflect genuine surface interactions rather than velocity-dependent hydrodynamic effects. Moreover, Figure S5c raises the question of whether the continuous motion at average velocity  $v_{\text{avg}} = \Delta\delta/\tau$  would be equivalent to the stepped protocol. The comparison reveals a striking difference: at equivalent average velocity, a stepwise displacement consistently produces smaller forces, with differences being most pronounced at large separations—precisely the distance range where the zero-force level is determined. For instance, at  $D = 20$  nm, the continuous motion yields  $F/R \approx 0.12$  mN/m compared to  $\approx 0.08$  mN/m for the stepped movement. This occurrence results from the delays that provide discrete relaxation windows for the system to attain equilibrium through the exponential factor  $\exp[-K\tau/\lambda(D)]$ . As long as the delay  $\tau$  exceeds several characteristic times  $\tau_{\text{relax}}(D) = \lambda(D)/K$ , the cantilever will have returned close to equilibrium before the next step occurs. The stepped protocol thus acts as a low-pass filter, attenuating fast hydrodynamic responses while preserving slower surface force contributions. For measuring true equilibrium forces, the stepwise protocols with adequate equilibration times are not merely being convenient, they are necessary, since continuous motion systematically overestimates forces due to unrelaxed hydrodynamic contributions.

Figure S5d illustrates the core of our proposed methodology allowing the motion to be modified at any surface separation. Here the force profile is calculated when at large separations the moving surface traveling at high speed ( $v = 0.265$  nm/s) is suddenly slowed down by a factor  $\sim 25$  ( $v = 11$  pm/s). In this illustration, the modification of the effective velocity occurs at  $D = 60$  nm. Remarkably, the force profile catches up its new characteristic response in only 3 incremental steps of displacement. This rapid convergence establishes that the system responds shortly and does not keep memory of previous measurements. This behavior is generic of viscous fluids under confinement: at any separation the force depends mainly on the current protocol parameters, which validates the processing of each measurement point as being independent. Most importantly, with that factual finding in hand, one can proceed with an analysis of the terms of the procedure and draw some conclusions and lines of conduct. It appears that extremely slow surface motions are unnecessary at large separations where surface forces are weak. For this liquid viscosity, the calculation shows that faster protocols are sufficient for  $D > 60$  nm. Conversely at smaller separations, the need of accurate measurements is essential and requires more than just slow movements: long equilibration times are also needed because nanostructural rearrangements proceed slowly, requiring the system to fully relax and to equilibrate at each distance step. Thanks to such a protocol optimization the total measurement duration can thus be reduced from 12 hours to 4–5 hours without affecting accuracy in critical regions.

In summary, the numerical simulations led to several findings. First, it is established that hydrodynamic minimization is achievable with appropriate protocol parameters. Second, through their periodic relaxation, the stepwise protocols are inherently superior to continuous motion. Third, the subtle effects induced by the way the moving surface is actuated explain the literature discrepancies in the reported magnitude of the screening lengths. The strong dependence on measurement conditions—spanning two orders of magnitude in hydrodynamic contribution—clarifies why different groups have reported widely varying results. Fast protocols systematically overestimate the force ranges due to unrelaxed contributions, creating the illusion of anomalously long-range interactions. The rapid force profile convergence when one passes from one protocol to another validates the dependence of measured forces upon the instantaneous conditions only. This supports the assumption that hydrodynamic and surface forces contribute to the total force almost additively. Most importantly, this analysis confirms the core claim of the main text. Once hydrodynamic contributions are unambiguously separated and/or minimized through rigorous experimental protocols—as demonstrated here with both techniques—long-range forces may arise from non-equilibrium states in the confined ILs. These apparent measured long-range interactions are inclined to vanish when the confinement gap thickness is reduced more slowly with concomitantly longer equilibration times, although there may remain some additional slow dynamic effects (Figures 1 and 2 of the main text; Figure S6: see Sec. 5.1). In contrast, at sufficiently slow velocities with adequate equilibration times, the screening lengths do converge to values consistent with theoretical predictions

for ionic liquids.

## INTERPLAY OF HYDRODYNAMIC AND SURFACE FORCES CONTRIBUTIONS

### Effect on the structural forces

This section examines the effect of velocity and resting time on the structural forces and their hysteresis between approach and retraction of surfaces confining ionic liquid films. The measured force profiles deviate from the expected drainage of a thin liquid film between solid extended surfaces (Figure 2 (main text) and Figures S1–S3, S5), despite the confirmation that the IL maintains constant bulk viscosity up to the shear plane and though inertial and acceleration effects are negligible given low Reynolds numbers ( $Re \ll 10^{-4}$ ). Even after velocity normalization, small but persistent discrepancies remain visible in Figure S3. These observations indicate that the interactions measured at distances preceding the structural force regime depend on velocity, even in the absence of acceleration or inertial effects. The standard procedure of subtracting the calculated hydrodynamic contributions from the total measured forces to obtain the surface forces assumes that surface velocities are sufficiently slow for equilibrium conditions to prevail [31]. However, the persistence of some velocity-dependent discrepancies questions not only this assumption but also the validity of considering surface forces as simple additive interactions to the velocity-dependent contribution when interpreting the total measured force, as presented here for structural forces.

As illustrated in Figure S6, our observations evidence a complex IL behavior under confinement and stress, with a subtle interplay between resting time and solvation (structural) forces when comparing the force-distance profiles at increasing velocities. While faster movements generate larger hydrodynamic contributions causing the total force magnitude to increase at large separations in the absence of solvation forces, the latter may conversely prevail at small gaps resulting in higher measured forces despite slower surface motion (blue losanges, fast speed vs. brown circles, high speed). Faster movements give the confined IL less time to undergo structural rearrangements and layering buildup. As a result, the compressive energy barrier to squeeze out any layer in formation is lowered and the related oscillation in the force profile reduces its height or may even disappear. Such scenarios, that were already observed in other fragile systems such as sponge and lamellar mesophases [38–41] and in thin films [22, 44–46, 49, 50, 52–54], underline the importance of conducting force measurements under conditions as close as possible to thermodynamic equilibrium.

Another observation is the velocity-dependent extent of the structured region. Comparing Figure 1 (main text, “very slow” speed) with Figure S6 reveals that the structural oscillations begin at  $D \sim 8\text{--}9$  nm for the slowest approach, but only below  $D \sim 4\text{--}5$  nm at higher velocities. This systematic increase in the thickness of the layered region with decreasing velocity underscores the need of finite relaxation times for the IL to build its structure under confinement. At faster approaches, the confined liquid has insufficient time to develop the full extent of layering, resulting in a compressed structural regime. This velocity-dependent structural thickness provides another direct evidence for the non-equilibrium nature of force measurements at high approach rates.

The last striking feature is the non-reversibility in the oscillatory regime upon reversal of the movement. This occurs even at the slowest possible velocity as illustrated by the semi-log and linear scales of the force-distance profile that was continuously measured upon approach of the surfaces and then upon separation (Fig. 1 bottom, main text). Such observations suggest that at small gaps the strain field generated by a change in the separation between two hard walls [55] does not induce a pure elastic response of the confined IL. Three arguments advocate for this conclusion. The first two remarks are related to the shape of the oscillations. Although the force profile consists of successive parts with magnitude and slope increasing as the surface separation  $D$  decreases, the oscillations, though non-linear in shape, are not parabolae. Secondly, the symmetry of each oscillation is broken relatively to its minimum. The inside and the outside of the oscillations appear well differentiated with continuous distortion of the shape especially upon decompression. Thus, the outward jumps (for instance, observed at  $D \sim 4.1$  and  $\sim 5.4$  nm for the 3rd and 4th oscillation respectively) may occur at locations further away from the expected oscillations minima (that should lie at grossly mid-distances between two adjacent maxima [38–42, 56]). In addition, one has noted that the history of the sample under study is of importance as both magnitude and shape of the oscillations may depend on the number of cycles (load/unload) previously performed at the same contact position. This echoes the third argument bringing the mechanical instability occurrence (inward and outward jumps) into scrutiny about their regularity at a given velocity. Contrary to outward jumps with no regular positions, the location of the inward jumps as a function of their rank becomes almost linear upon increasing slowdown: the periodicity,  $d$ , approaches a value around 0.8 nm as inferred from the slope of the line of best fit. This  $d$  value is in agreement with the short-range ordering periodicity reported previously by AFM [57] and SFA [58] and corresponds to the dimensions of an ion pair. All three sets of remarks

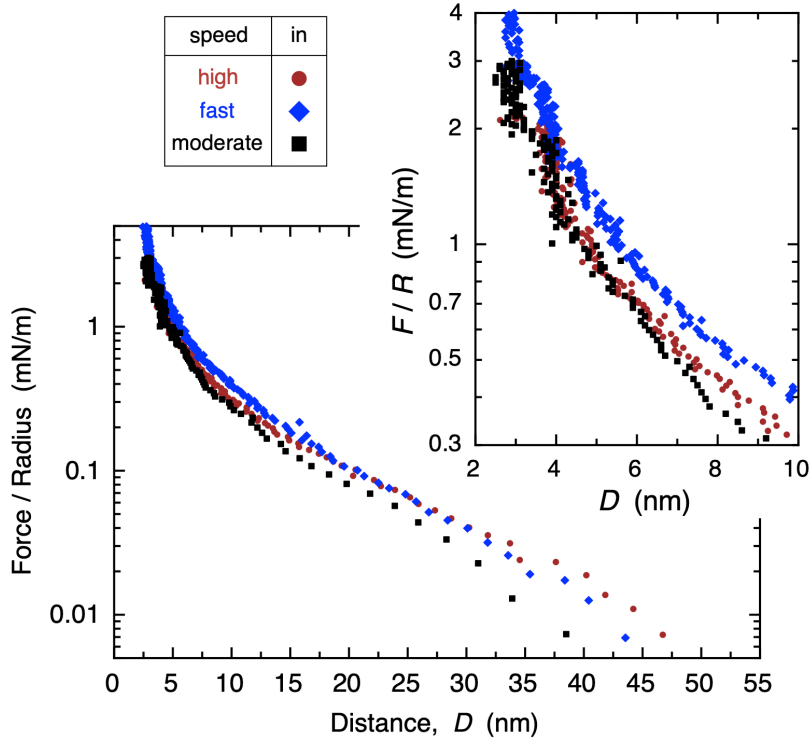


FIG. S6. Force-distance profiles for  $[\text{C}_2\text{mim}][\text{NTf}_2]$  confined between crossed mica cylinders at different approaching motion conditions of the surfaces at high (brown circles), fast (blue losanges) and moderate (black squares) speeds (data from Fig. 1, main text, with corresponding experimental conditions reported in Fig. S5b). The force-distance profiles are composed of two distinct regimes with spatial extent and magnitude both depending on velocity, stepwise and resting time conditions for surface movements (all parameters reported in Sec. 4, SI). At large separations the interactions are all monotonic repulsive and reversible (see main text). At short separations the oscillatory functions of distance are prominently related to the structuration of the IL that may not be reversible upon decompression. They lie on a repulsive background resulting from the interplay of two effects. Faster movements induce larger hydrodynamic repulsions, but instead give the confined IL less time to undergo structural rearrangements and layering buildup. As a result, the compressive energy barrier to squeeze out any layer in formation is lowered and the related oscillation in the force profile reduces its height or may even disappear. This competitive effect is illustrated (inset) by comparing the forces collected at the highest velocity (brown circles, high speed) that have a smaller magnitude (at small separations) with the force collected at a slower velocity (blue squares, fast speed).

harmonize with respect to claiming that the IL film is microstructured with bare mica, becomes anisotropic with layering buildup upon confinement, but does not behave as a smectic phase. Otherwise, its elastic energy would be lowered by the introduction or the loss of a layer depending on the sign of the applied external strain: the relaxation would occur by edge dislocations [56]. Here, the compressive forces follow a path deviating from a pure elastic parabolic shape, a path likely to run above the supposed set of intersecting parabolae [56]. On dilation another path is followed, and even if edge dislocations might exist, their annihilation is not equivalent to their creation. Actually, as pointed out by de Gennes [59], some of the defects may bear little resemblance to dislocations in bulk, as the core region may be spread along the plane of the layers to such an extent that the concept of a dislocation line is no longer applicable [55, 59–62]. In the experimental wedge geometry of two crossed cylinders, it may be energetically less costly to have continuously distorted layers contouring the curved walls. Whatever the cause, our observations suggest plastic contributions to the net force and different activation barriers and delays to squeeze out or incorporate a layer in the confined medium that involve structural rearrangements and energetic changes which are propagating from the nucleation site throughout the thin film, and occur within transit times.

As a result, the structural forces are intrinsically velocity-dependent—not through an additive velocity-correction force (the viscosity remains constant as demonstrated in Sec. 3.2 and viscous contributions are reliably calculated), but because the force reflects the actual reorganization state at each measurement timescale. In fact, the velocity-dependence occurs even if one considers pure elastic behaviors only. This is for instance the case of confined smectic mesophases, as first discussed by Pershan and Prost when an external strain is applied to a smectic confined between two parallel rigid walls. The relaxation of the induced elastic stress occurs by edge dislocation loops. Transit times

are involved as the nucleation process follows a Poisson-Boltzmann distribution with a nucleation rate of stable loops scaling as  $\exp(-E_c/k_B T)$  in which  $E_c$  is the energy barrier of the loop to overcome a critical pore radius for formation and growth. In a confined medium of non-uniform thickness, such as a sphere against a flat plane (or equivalently two crossed cylinders), an array of dislocations builds [63]. In the wedge-shaped geometry, the strain field decays as  $\exp(-x^2/\xi z)$  where  $\xi$  is the penetration length and  $x$  and  $z$  are the coordinates parallel and perpendicular to the layers, respectively, according to de Gennes [59, 61]. The range of the strain field is about that of the penetration length, that is a few reticular distances. For the ILs investigated in this work,  $\xi$  would be a few nanometers as the reticular distance is  $d \sim 0.8$  nm (see Table S1, Sec. 1 SI, and refs. [57, 58]). Thus, any change in the wall-separation induces perturbations not only on the wedge confinement energy due to the elastic stress of the layered material, but also on the line tensions associated to each loop, through the core of the defect itself and the far-field energy from the distortion field around the dislocation core [55]. The speed of the moving surface that changes the gap thickness between the confining walls was shown to be crucial [64–66]. Some numerical considerations about the dynamics have also been discussed previously in the same crossed-cylinder SFA geometry [56]. Yet the concern about the achievement of thermodynamic equilibrium was emphasized for sound interpretation of experimental observations, rather than dealing with marked non-equilibrium effects. The additional complication due to plastic contributions has also been reported in several systems: a set of various time relaxations was evidenced [43, 67], but also additional slippage events and tapering off to a background drift rate over a period of tens of seconds with cascades of instabilities [67].

Before concluding this section, a final remark. Note that in the short-range separation regime, the force profiles are presented (main text) upon inwards and outwards surface movements only from large separations to contact or the converse, with no reversed movement actuated at intermediate separations. This is because the focus of the work was to investigate the nature and the range of the long-range monotonic repulsion rather than an investigation of the solvation structural forces at short separations. Therefore, we have not sought to recover the inaccessible regions due to the mechanical instability that causes the surfaces to jump to a new equilibration separation where the gradient of the force is less than the cantilever spring constant,  $K$ . This would have implied to perform multicycles where the surfaces are brought together, stopped at specific separations, and then moved outwards to pass the minimum in force, allowing the position and depth of each oscillation to be determined, as Perkin’s group reported [58]. Note also that in all our measurements, the maximum compressive force  $F/R$  remains below 10 mN/m to avoid artefacts due to the deformation of the glue beneath the mica sheet [28, 29] (see also Sec. 2)—a value to be compared to more than 30 mN/m in Perkin’s report (Fig. 2 in ref. [58]). This difference indicates that we remained in a regime where repulsive structural forces are still dominant, but have expelled the outermost few layers only. Therefore, the force minima in Figure 1 (main text) cannot be compared to the ones reported for instance in ref. [58]. Nevertheless, at very slow speed, the magnitude of  $F/R \approx -0.05$  mN/m remains consistent with the last minimum reported in Figure 2 of reference [58].

In conclusion, structural forces build force-distance profiles that may be affected by motion conditions of the moving confining surface. Plastic contributions to the net force, different activation barriers, delays and transit times to squeeze out or incorporate layers involving structural rearrangements and energetic changes, and dependence on confining wall velocity all demonstrate that the measured structural forces depend strongly on experimental conditions. Faster approaches yield lower energy barriers (incomplete layering) while slower approaches allow higher barriers to be built (more complete organization). This behavior, well documented in liquid crystals and confined systems, reflects a fundamental coupling between measurement protocols and structural states. As a result, caution is advised regarding the usual way of considering surface forces as simple additive interactions to the hydrodynamic contribution for interpreting the total measured force, because other velocity dependence effects are left apart. Only under quasi-static conditions do the structural forces converge toward their equilibrium distance profiles.

### Hydrodynamic vs. electrostatic force contributions

The relative importance of hydrodynamic and electrostatic contributions is examined through a dimensionless analysis applicable to all constant-velocity measurement protocols. This framework is relevant not only to the dSFA experiments presented here, but also to conventional SFA and AFM techniques employing continuous surface displacement. The dimensionless number  $\Pi$  derived below provides a universal criterion for assessing which force regime dominates under given experimental conditions:

$$\Pi = \frac{6\pi\eta Rv}{Z\kappa_D^{-1} \exp(-\kappa_D D)} \quad (\text{S5})$$

This number is the ratio between the drag viscous force  $F_h = 6\pi\eta R^2 v/D$  and the electrical double layer interaction

$F_e$  acting at large separations, that has a magnitude related to the surface potential,  $\psi_0$ , at the onset of the electrical double layer, and decays exponentially asymptotically with a screening length  $\kappa_D^{-1}$  as  $F_e = Z\kappa_D^{-1} \exp(-\kappa_D D)$  where  $Z = 64\pi R\epsilon_0\epsilon_r(k_B T/e)^2 \tanh^2(e\psi_0/4k_B T)$ . For  $\Pi$  larger than one, the hydrodynamic interaction dominates while the electrostatic force dominates for  $\Pi$  smaller than one.

The equation  $\Pi = 1$  is solved numerically for different ratio values  $6\pi\eta Rv/Z$  to find the solutions in terms of  $\kappa_D D$ . The solutions, if they do exist, lead to the distance range regime where the electrostatic interactions may dominate the hydrodynamic forces, that is the surface separations range over which electrostatic interactions can be measured. Figure S7 represents the phase diagram in the coordinates  $6\pi\eta Rv/Z$  versus  $\kappa_D D$  for  $[\text{C}_4\text{mim}][\text{PF}_6]$  with viscosity  $\eta = 157 \text{ mPa}\cdot\text{s}$  [1], dielectric constant  $\epsilon = 11.4$  [15, 16], and surface potential  $|\psi_0| = 16 \text{ mV}$  (see main text). The dashed line is the representative curve of  $\Pi = 1$  in this coordinate system. If the ratio  $6\pi\eta Rv/Z$  is larger than  $\exp(-1) \approx 0.37$ , the equation  $\Pi = 1$  has no solution and the hydrodynamic force is always larger, at any distances, than the electrostatic interaction. For lower values of the ratio, the equation  $\Pi = 1$  has two solutions and electrostatic interactions are larger than hydrodynamic forces for distances in the interval given by the two solutions  $D_-$  and  $D_+$ , with  $D_- < D_+$ . For distances  $D$  larger than  $D_+$ , the exponential forces are weaker than the hydrodynamics forces.

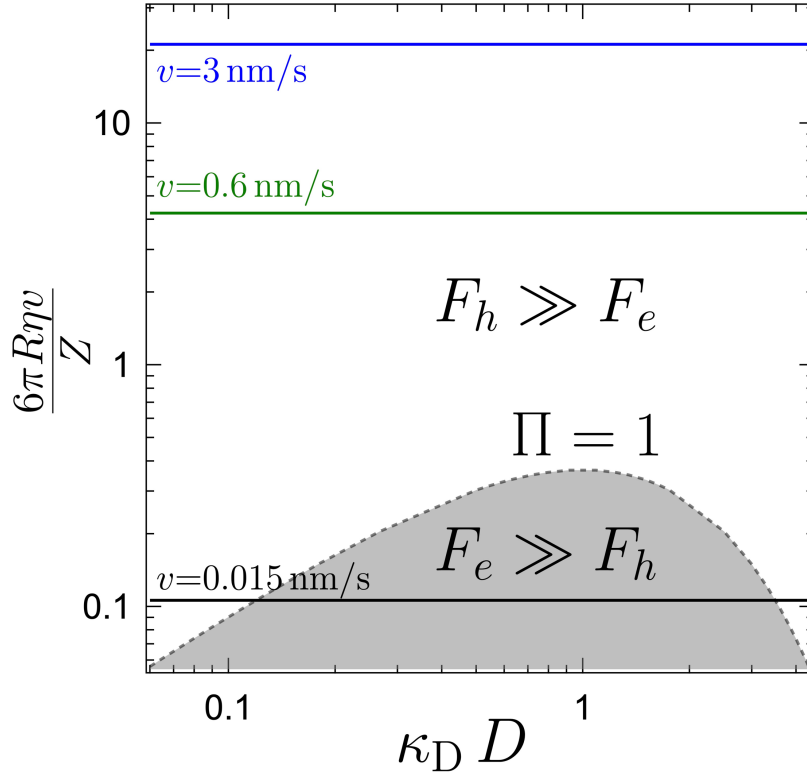


FIG. S7. Phase diagram defining force dominance regimes. Dimensionless parameter  $6\pi\eta Rv/Z$  versus  $\kappa_D D$  shows hydrodynamic-dominated (white,  $F_h \gg F_e$ ) and electrostatic-dominated (grey,  $F_e \gg F_h$ ) regions separated by the  $\Pi = 1$  boundary (dashed line). Horizontal lines represent experimental velocities of 3.0 nm/s (blue), 0.6 nm/s (green), and 0.015 nm/s (black), illustrating the accessibility of electrostatic measurements at the lowest velocity.

The practical measurement of exponential forces superimposed on hydrodynamic contributions requires careful consideration of the relative magnitude of the competing interactions. As illustrated in Figure S7, reliable detection of electrostatic forces necessitates that  $F_e$  exceeds  $F_h$  which defines the accessible measurement window in terms of  $\kappa_D D$ . This criterion ensures that the exponential contribution can be unambiguously distinguished from the underlying hydrodynamic baseline and that accurate force decomposition is achievable.

Several important consequences and outputs emerge from this analysis.

First, the assumption of additive force contributions has been adopted throughout this study. While this assumption appears reasonable as a starting point, the results from Sec. 3.2 and particularly Sec. 4 indicate that hydrodynamics—or at minimum the velocity  $v$ —influences the force profile. This influence, through a coupling between forces, suggests opportunities for refining this assumption in future work.

Second, by adopting the force additivity assumption (following protocols established for dSFA data analysis),

behaviors exhibiting like-exponential characteristics have been identified. At the slowest velocities, the measurements span two orders of magnitude in force, and the collected data yield particularly rich insights: there the exponential nature of the surface force profiles becomes unambiguous and reliable. At intermediate velocities of 3 nm/s and 0.6 nm/s, some exponential expressions could be inferred despite noisier data and a more limited force range (spanning only one order of magnitude; see Figure 2, main text). Under these conditions, the exponential character becomes less definitive, and power-law fits would provide comparable quality, highlighting the inherent flexibility in modeling approaches. Even if successful, the exponential interpretation proposed by others (see main text) using fits to large scattered force data and besides over one order magnitude only is not proven to be physically correct, or that other models could not be equally successful (and remain equally unproven!).

This versatility emphasizes the importance of advancing theoretical frameworks to clarify the fundamental mechanisms governing any long-range forces at intermediate velocity and to establish more robust functional forms. It should be noted that this constitutes an empirical modeling approach designed to describe the experimental data. Success in fitting does not establish the physical validity of the model, nor does it preclude other formulations from achieving comparable results.

Third, an interesting feature of hydrodynamic forces is their extremely long-range nature. As Figure S3 illustrates, with the force resolution of dSFA, the force remains measurable at half a micron away from surface contact. Since the technique determines forces by means of deflections of elastic elements, the choice of the reference point for defining the zero-force becomes an important methodological consideration. In previous IL works reported by other groups, the position of the reference point at which the zero force is chosen is not specified. As a consequence, the data analysis can be biased (for instance, setting the zero-force reference at 100 nm from surface contact implies to subtract the hydrodynamic force present at this distance from all subsequent measurements). Conversely, in the current study, such biased analysis is avoided. Here, the force baseline was established by averaging the measured force over the interval from 0.8 to 1.0  $\mu\text{m}$ , where forces are minimal and stable, thus providing a robust reference point.

---

\* benjamin.cross@univ-grenoble-alpes.fr

† patrick.kekicheff@ics-cnrs.unistra.fr

- [1] G. Yu, D. Zhao, L. Wen, S. Yang, and X. Chen, *AIChE J.* **58**, 2885 (2012).
- [2] A. P. Fröba, H. Kremer, and A. Leipertz, *J. Phys. Chem. B* **112**, 12420 (2008).
- [3] M. G. Montálban, C. L. Bolívar, F. G. Díaz Baños, and G. Villora, *J. Chem. Eng. Data* **60**, 1986 (2015).
- [4] B. L. Bhargava, R. Devane, M. L. Klein, and S. Balasubramanian, *Soft Matter* **3**, 1395 (2007).
- [5] W. M. Reichert, J. D. Holbrey, R. P. Swatloski, K. E. Gutowski, A. E. Visser, M. Nieuwenhuyzen, K. R. Seddon, and R. D. Rogers, *Cryst. Growth Des.* **7**, 1106 (2007).
- [6] C. Song, P. Wang, and H. A. Makse, *Nature* **453**, 629 (2008).
- [7] A. A. Lee, D. Vella, S. Perkin, and A. Goriely, *J. Phys. Chem. Lett.* **6**, 159 (2015).
- [8] J. M. Slattery, C. Daguinet, P. J. Dyson, T. J. Schubert, and I. Krossing, *Angew. Chem. Int. Ed.* **119**, 5480 (2007).
- [9] K. Fujii, Y. Soejima, Y. Kyoshoin, S. Fukuda, R. Kanzaki, Y. Umebayashi, T. Yamaguchi, S. Ishiguro, and T. Takamuku, *J. Phys. Chem. B* **112**, 4329 (2008).
- [10] I. Billard, G. Moutiers, A. Labet, A. El Azzi, C. Gaillard, C. Mariet, and K. Lützenkirchen, *Inorg. Chem.* **42**, 1726 (2003).
- [11] A. Triolo, A. Mandanici, O. Russina, V. Rodriguez-Mora, M. Cutroni, C. Hardacre, M. Nieuwenhuyzen, H.-J. Bleif, L. Keller, and M. A. Ramos, *J. Phys. Chem. B* **110**, 21357 (2006).
- [12] J. N. A. Canongia Lopes and A. A. H. Pádua, *J. Phys. Chem. B* **110**, 3330 (2006).
- [13] A. Triolo, O. Russina, B. Fazio, R. Triolo, and E. Di Cola, *Chem. Phys. Lett.* **457**, 362 (2008).
- [14] D. Xiao, L. G. Hines, S. Li, R. A. Bartsch, E. L. Quitevis, O. Russina, and A. Triolo, *J. Phys. Chem. B* **113**, 6426 (2009).
- [15] H. Weingärtner, *Angew. Chem. Int. Ed.* **47**, 654 (2008).
- [16] M. Mizoshiri, T. Nagao, Y. Mizoguchi, and M. Yao, *J. Chem. Phys.* **132**, 164510 (2010).
- [17] J. N. Israelachvili and D. Tabor, *Proc. R. Soc. Lond. A* **331**, 19 (1972).
- [18] J. N. Israelachvili and G. E. Adams, *J. Chem. Soc. Faraday Trans. 1* **74**, 975 (1978).
- [19] L. Garcia, C. Barraud, C. Picard, J. Giraud, E. Charlaix, and B. Cross, *Rev. Sci. Instrum.* **87**, 113906 (2016).
- [20] C. Barraud, L. Garcia, B. Cross, and E. Charlaix, *Meas. Sci. Technol.* **28**, 045103 (2017).
- [21] P. Kékicheff, in *Electrostatic Effects in Soft Matter and Biophysics*, NATO Science, Series II—Mathematics Physics and Chemistry, Vol. 46, edited by C. Holm, P. Kékicheff, and R. Podgornik (NATO, 2001) pp. 205–281.
- [22] P. Kékicheff, *Adv. Colloid Interface Sci.* **270**, 191 (2019).
- [23] S. Tolansky, *An introduction to Interferometry*, 2nd ed. (Longmans, London, 1973).
- [24] J. N. Israelachvili, *J. Colloid Interface Sci.* **44**, 259 (1973).
- [25] R. G. Horn and D. T. Smith, *Appl. Opt.* **30**, 59 (1991).
- [26] P. Kékicheff and O. Spalla, *Langmuir* **10**, 1584 (1994).
- [27] M. Born and E. Wolf, *Principles of Optics* (Pergamon Press, Oxford, 1959).

- [28] P. Attard and J. L. Parker, *Phys. Rev. A* **46**, 7959 (1992).
- [29] J. L. Parker and P. Attard, *J. Phys. Chem.* **26**, 10398 (1992).
- [30] B. V. Derjaguin, *Kolloid Z.* **69**, 155 (1934).
- [31] D. Y. C. Chan and R. G. Horn, *J. Chem. Phys.* **83**, 5311 (1985).
- [32] L. Garcia, L. Jacquot, E. Charlaix, and B. Cross, *Faraday Discuss.* **206**, 443 (2018).
- [33] S. Leroy and E. Charlaix, *J. Fluid Mech.* **674**, 389 (2011).
- [34] L. Bocquet and E. Charlaix, *Chem. Soc. Rev.* **39**, 1073 (2010).
- [35] I. Bou-Malham and L. Bureau, *Soft Matter* **6**, 4062 (2010).
- [36] K. Ueno, M. Kasuya, M. Watanabe, M. Mizukami, and K. Kurihara, *Phys. Chem. Chem. Phys.* **12**, 4066 (2010).
- [37] R. Lhermerout and S. Perkin, *Phys. Rev. Fluids* **3**, 014201 (2018).
- [38] D. A. Antelmi, P. Kékicheff, and P. Richetti, *J. Phys. II France* **5**, 103 (1995).
- [39] D. A. Antelmi and P. Kékicheff, *J. Phys. Chem. B* **101**, 8169 (1997).
- [40] E. Freyssingeas, D. Antelmi, P. Kékicheff, P. Richetti, and A.-M. Bellocq, *Eur. Phys. J. B* **9**, 123 (1999).
- [41] D. A. Antelmi, P. Kékicheff, and P. Richetti, *Langmuir* **15**, 7774 (1999).
- [42] L. Herrmann, A. Johner, and P. Kékicheff, *Phys. Rev. Lett.* **113**, 268302 (2014).
- [43] L. Herrmann and P. Kékicheff, *Macromol. Symp.* **359**, 88 (2016).
- [44] Á. Kulcsár, P. Lavalle, J.-C. Voegel, P. Schaaf, and P. Kékicheff, *Langmuir* **20**, 282 (2004).
- [45] Á. Kulcsár, J.-C. Voegel, P. Schaaf, and P. Kékicheff, *Langmuir* **21**, 1166 (2005).
- [46] M. Bauer, P. Kékicheff, J. Iss, C. Fajolles, T. Charitat, J. Daillant, and C. M. Marques, *Nat. Commun.* **6**, 8117 (2015).
- [47] D. Atkins, P. Kékicheff, and O. Spalla, *J. Colloid Interface Sci.* **188**, 234 (1997).
- [48] O. Spalla and P. Kékicheff, *J. Colloid Interface Sci.* **192**, 43 (1997).
- [49] P. Kékicheff, G. F. Schneider, and G. Decher, *Langmuir* **29**, 10713 (2013).
- [50] P. Kékicheff, *Macromol. Symp.* **335**, 24 (2014).
- [51] M. A. Gebbie, H. A. Dobbs, M. Valtiner, and J. N. Israelachvili, *Proc. Natl. Acad. Sci. U.S.A.* **112**, 7432 (2015).
- [52] P. Kékicheff, F. Nallet, and P. Richetti, *J. Phys. France II* **4**, 735 (1994).
- [53] P. Kékicheff, J. Iss, P. Fontaine, and A. Johner, *Phys. Rev. Lett.* **120**, 118001 (2018).
- [54] P. Kékicheff and C. Contal, *Langmuir* **35**, 3087 (2019).
- [55] M. Kléman, *Points, Lines and Walls: In Liquid Crystals, Magnetic Systems, and Various Ordered Media* (Wiley, New York, 1983).
- [56] P. Richetti, P. Kékicheff, and P. Barois, *J. Phys. II France* **5**, 1129 (1995).
- [57] Z. Wang, H. Li, R. Atkin, and C. Priest, *Langmuir* **32**, 8818 (2016).
- [58] A. M. Smith and S. Perkin, *J. Phys. Chem. Lett.* **6**, 4857 (2015).
- [59] P.-G. de Gennes, *C. R. Acad. Sci. (Paris) B* **275**, 939 (1972).
- [60] M. Kléman, *J. Phys. France* **35**, 595 (1974).
- [61] P.-G. de Gennes and J. Prost, *The Physics of Liquid Crystals*, 2nd ed. (Clarendon Press, Oxford, 1993).
- [62] K. M. McGrath, P. Kékicheff, and M. Kléman, *J. Phys. II France* **3**, 903 (1993).
- [63] W. K. Chan and W. W. Webb, *J. Phys. (France)* **42**, 1007 (1981).
- [64] P. Oswald, *Crystals* **9**, 44 (2019).
- [65] P. Oswald and P. Pieranski, *Nematic and Cholesteric Liquids Crystals: Concepts and Physical Properties Illustrated by Experiments* (Taylor & Francis, Boca Raton, FL, 2005).
- [66] P. Oswald and P. Pieranski, *Smectic and Columnar Liquids Crystals: Concepts and Physical Properties Illustrated by Experiments* (Taylor & Francis, Boca Raton, FL, 2006).
- [67] R. A. Herke, N. A. Clark, and M. A. Handschy, *Phys. Rev. E* **56**, 3028 (1997).